Line-Field Spectral Domain Optical Coherence Tomography: Design and Biomedical Applications

by

Keyu Chen

A thesis

presented to the University of Waterloo

in fulfillment of the

thesis requirement for the degree of

Master of Science

in

Physics

Waterloo, Ontario, Canada, 2024

Author's Declaration

This thesis consists of material all of which I authored or co-authored: see Statement of Contributions included in the thesis. This is a true copy of the thesis, including any required final revisions, as accepted by my examiners.

I understand that my thesis may be made electronically available to the public.

Statement of Contributions

Chapter 3:

Keyu Chen, Weixiang Song, Le Han, and Kostadinka Bizheva. "Powell lens-based line-field spectral domain optical coherence tomography system for cellular resolution imaging of biological tissue," Biomed. Opt. Express 14, 2003-2014 (2023)

Keyu Chen and Kostadinka Bizheva conceived the study.

Kostadinka Bizheva provided the study material.

Weixiang Song and Le Han programmed the LabVIEW control software, and provided general feedbacks to the study.

Keyu Chen designed, built, and characterized the system, wrote data processing algorithms.

Keyu Chen and Kostadinka Bizheva conducted the plant tissue and animal tissue image sessions.

Keyu Chen processed data, prepared figures, and wrote the draft manuscript.

Kostadinka Bizheva revised the manuscript.

All authors contributed to the final version of the manuscript.

Chapter 4:

Keyu Chen, Nima Abbasi, Julian Parkin, Alex Wang, and Kostadinka Bizheva. "Powell lens-based Line-Field OCT for in-vivo, contact-less, cellular resolution imaging of the human cornea," (submitted to Biomedical Optics Express, under review)

Keyu Chen and Kostadinka Bizheva conceived the study.

Kostadinka Bizheva provided the study material.

Julian Parkin updated existing LabVIEW code to allow for integration of PCO CS4 camera.

Keyu Chen designed, built, and characterized the system, wrote data processing algorithms.

Keyu Chen and Kostadinka Bizheva conduced the in-vivo human imaging sessions.

Nima Abbasi and Alex Wang developed a new image processing code to sharpen OCT images. The code was used to process the human cornea LS-OCT images.

Keyu Chen processed data, prepared figures, and wrote the draft manuscript.

Kostadinka Bizheva revised the manuscript.

All authors contributed to the final version of the manuscript.

Chapter 5:

Keyu Chen, Stephanie Swanson and Kostadinka Bizheva, "Line-Field dynamic Optical Coherence Tomography platform for assessment of biological tissues," (submitted to Biomedical Optics Express, under review)

Keyu Chen and Kostadinka Bizheva conceived the study.

Kostadinka Bizheva provided study material.

Julian Parkin and **Keyu Chen** wrote the camera LabVIEW control software.

Keyu Chen designed, built, and characterized the system, wrote data processing and dynamic processing algorithms.

Stephanie Swanson prepared tumor spheroids samples.

Keyu Chen and Stephanie Swanson conducted the image sessions.

Keyu Chen processed data, prepared figures, and wrote the draft manuscript.

Kostadinka Bizheva revised the manuscript.

All authors contributed to the final version of the manuscript.

Abstract

Corneal diseases such as keratoconus and Fuchs' dystrophy lead to the dysfunction of the cornea, which can result in vision loss. Early-stage detection at the cellular level provides the opportunity for treatment that slows or stops disease progression and potentially for disease cure. Optical coherence tomography (OCT), often described as the optical equivalent of ultrasound imaging, enables high-speed, non-invasive volumetric imaging at a cellular resolution. These advantages of OCT have made it a useful tool in ophthalmology and beyond. High-speed OCT data acquisition is desirable, particularly for volumetric imaging, to reduce involuntary eye and body motion and suppress motion-induced artifacts. Line-scan OCT (LS-OCT) utilizes a 2D lens, such as a cylindrical lens, as the line generator to project a line-shaped detection beam onto the sample instead of the focused pencil beam traditionally used in OCT systems. Combined with high-speed 2D cameras, LS-OCT systems allow for a data acquisition speed that is 1 to 2 orders of magnitude higher than conventional point-scanning OCT systems. The three main goals of this thesis research are: (i) to develop a novel Powell lens-based line-scan OCT system, (ii) to optimize the performance of the Powell lens-based line-scan OCT system for in vivo human studies, and (iii) to develop a line-scan OCT protocol for conducting dynamic OCT (dOCT) studies on various biological tissues.

A Powell lens is used in a line-field spectral domain OCT (PL-LF-SD-OCT) system to generate a line-shaped imaging beam with an almost uniform distribution of optical power along the line direction. This design overcomes the significant sensitivity loss of approximately 10 dB that is observed along the line length direction (B-scan) in LF-OCT systems based on cylindrical lens line generators. The PL-LF-SD-OCT system offers almost isotropic spatial resolution (Δx and Δy approximately 2 μm, Δz approximately 1.8 μm) in free space and a sensitivity of approximately 87 dB with only about 1.6 dB loss along the line length for an imaging power of 2.5 mW at an imaging rate of 2,000 frames per second (fps). Images acquired with the PL-LF-SD-OCT system allow for the visualization of cellular and sub-cellular structures of biological tissues.

Following the development of the first PL-LF-OCT system, we present a second-generation system that combines sufficiently high: spatial resolution (2.4 μm × 2.2 μm × 1.7 μm (x × y × z)) to resolve individual cells; sensitivity (approximately 90 dB) to image the semi-transparent human cornea; and image acquisition rate ($\geqslant$ 2,400 fps) to suppress most involuntary eye motion artifacts. In summary, the second-generation system allows for contactless, in vivo imaging of the cellular structure of the

human cornea. Volumetric images acquired in vivo from the corneas of healthy subjects show corneal epithelial, endothelial, and keratocytes cells, as well as sub-basal and stromal corneal nerves. The system's high axial resolution also allows for clear identification and morphometry of the corneal endothelium, Descemet's membrane, and the pre-Descemet's (Dua) layer.

By characterizing time-dependent signal intensity fluctuations, dOCT enhances contrast in OCT images and indirectly probes cellular metabolic processes. Almost all of the dOCT studies published so far are based on the acquisition of 2D dOCT images (B-scans or C-scans) via point-scanning spectral-domain/swept-source OCT or full-field OCT respectively, due to limitations in the image acquisition rate. Here we introduce a novel high-speed Line-Field dOCT (LF-dOCT) system and image acquisition protocols designed for volumetric dOCT imaging of biological tissues. The imaging probe is based on an exchangeable telecentric lens pair that enables a selection of transverse resolution (1.1 µm to 6.4 µm) and field of view (FOV) (250×250 µm² to 1.4×1.4 mm²) suitable for different biomedical applications. The system offers an axial resolution of 2.6 µm in free space, corresponding to approximately 1.9 µm in biological tissue assuming an average refractive index of 1.38. A maximum sensitivity of 90.5 dB is achieved for 3.5 mW optical power at the tissue surface and camera acquisition rate of 2000 fps. Volumetric dOCT images acquired with the novel LF-dOCT system from plant tissue (English cucumber) and animal tissues (mouse liver and prostate tumor spheroids) allow for volumetric visualization of the tissues' cellular and sub-cellular structure.

Acknowledgements

I want to begin by expressing my deepest gratitude to my supervisor, Prof. Bizheva, for her unwavering support throughout my MSc journey – academically, financially, and personally. I never anticipated working in the field of biomedical optics during my undergraduate studies, yet now, I am eager to continue my work in this exciting field in the future. Prof. Bizheva has granted me significant flexibility and freedom to explore various research topics. She has also provided me with numerous opportunities to present my research at different international conferences, which have been invaluable for learning from and networking with other distinguished researchers in the field. Dida, it has been a pleasure working with you over the past two and a half years.

I am also immensely thankful to Dr. Han Le and Song Weixiang, two former members of our lab. They have both provided me with an immense amount of support during our time together in the lab and thereafter. If I have seen further it is by standing on the shoulders of Giants. To all my colleagues in the lab, I appreciate the nurturing research environment we've cultivated together, and I wish you all the very best in your future research endeavors and life's journey.

To my friends in Canada and China, thank you for the joy and companionship you've brought into my life. Our shared years are treasured memories, and I eagerly anticipate the years yet to come.

Finally, to my parents: my heart is full of gratitude for your unconditional love and support. I embrace you with the biggest hug and all my love.

Table of Contents

List of Figures

Chapter 1
Introduction

1.1 Motivation

The cornea is the outermost layer of the eye and provides most of its optical magnification power. Healthy corneal function is crucial for allowing light to pass through efficiently and for focusing it properly on the retina [1]. Diseases such as keratoconus, which thins and reshapes the cornea from a dome to a cone shape [2], and Fuchs' dystrophy, which leads to corneal edema or dehydration due to the malfunction and death of corneal endothelial cells [3], both lead to vision loss. Cellular resolution imaging of the cornea is essential for the early-stage diagnosis of many corneal diseases, including the two mentioned above, as early symptoms typically appear at the cellular level. Conventionally, imaging techniques such as slit lamp imaging [1], ultrasound imaging [4], and in-vivo confocal microscopy (IVCM) [5,6] are utilized to examine the anterior segment of the eye. Slit lamp and ultrasound imaging both allow for non-invasive examination of the eye, although ultrasound imaging requires contact with the eyelid, so it is not perfectly non-invasive. IVCM provides cellular resolution imaging capability but requires direct contact between the microscopic objective and the eye tissues, which may result in potential damage to the eye, especially for those with unhealthy eye conditions. Using a low numerical aperture (NA) microscopic objective could make it possible to perform non-contact corneal imaging with IVCM, but this approach also sacrifices the spatial resolution of the system. Furthermore, the imaging acquisition speed of IVCM is normally limited, which presents an issue for volumetric in-vivo imaging due to involuntary body and eye movements.

Optical Coherence Tomography (OCT) serves as an alternative imaging technique for in-vivo, non-invasive, high-speed volumetric, cellular resolution eye imaging [7]. OCT has increasingly been used for ophthalmology diagnosis and academic research with the maturation of the technology in the three decades since its invention in 1991 [8]. The main objective of this thesis research is to continue the development of current OCT technology, specifically focused on the improvement of Line-Field OCT (LF-OCT), a parallel data collection OCT imaging modality which offers 1-2 orders of magnitude higher data acquisition speed compared to conventional clinical OCT systems [9-14]. The three specific goals outlining this MSc research are: 1) Investigate the possibility of using a Powell lens as a line-illumination generator for an OCT system, instead of conventionally using a cylindrical lens, for better light illumination uniformity in the line direction while still capable of achieving cellular resolution. 2) Investigate the possibility and outcomes of such a Powell-based LF-OCT system for in-vivo human

corneal imaging, with improved line-direction illumination uniformity from Powell lens while still taking advantage of the high speed of LF-OCT. 3) Investigate the possibility and outcomes of using an LF-OCT system to perform high-speed dynamic OCT (dOCT), an extension of conventional OCT which utilizing the temporal-dependent OCT signal fluctuations as an extra contrast, on various of ex-vivo and in-vitro biological tissues.

1.2 Cornea structures

The cornea is a transparent and vessel-free region of the anterior segment of the eye that functions to focus light onto the retina and to protect the inner eye structures from the environment. In a healthy human adult, the cornea typically has a thickness of approximately 500 μm to 600 μm near the apex, with an increased thickness up to about 640 μm towards the peripheral regions [15, 16]. Humans, as well as other primates, have a five-layered cornea comprising, from the anterior to posterior direction: the Epithelium, Bowman's layer, Stroma, Descemet's membrane, and Endothelium. Representative cross-sectional human cornea histology and OCT images are shown in Fig. 1. The anterior and posterior OCT corneal images are shown separately in Fig. 1(B) and 1(C) for more detailed views of local structures.

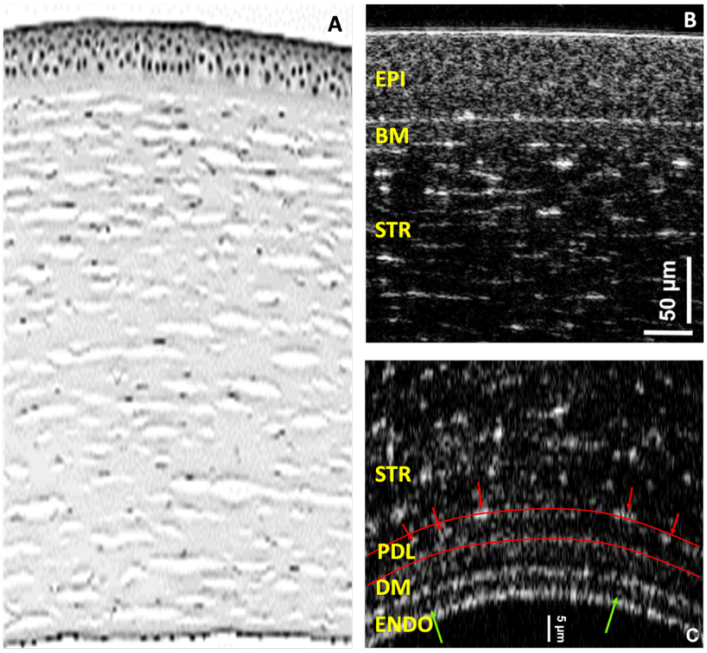

Fig. 1.1. (reproduced with permission from Prof. Denise Hileeto and Prof. Kostadinka Bizheva) (A) Histology image of health human cornea. (B) Anterior side of human cornea imaged in-vivo with

OCT cornea. EPI: Epithelium; BM: Bowman's membrane; STR: Stroma. (C) Posterior side of human cornea imaged in-vivo with OCT. PDL: pre-Descemet's layer; DM: Descemet's membrane; ENDO: Endothelium.

The epithelial layer consists of approximately six layers of cells. Starting from anterior to posterior, the three cell types are superficial cells (the oldest cells), wing cells, and basal cells (the youngest cells) [17]. The epithelial cells are highly regenerative with a vertical turnover rate of 7 to 14 days [18, 19]. The dying superficial cells are washed out by the tear film, which is situated directly above the superficial cell layer and also keeps the epithelium moist. The total thickness of the epithelium is approximately 40 μm to 50 μm in humans [20]. Bowman's layer, also known as the anterior limiting membrane, is an acellular region consisting primarily of collagen fibers and other proteins [21]. It serves the purpose of protecting the stroma and has a thickness of approximately 10 to 15 μm. It has been reported to slightly decrease in thickness with aging [22]. Unlike the epithelium, Bowman's layer does not regenerate [23]. The stroma is the middle layer of the cornea and contributes up to 90% of the cornea's total thickness. It is primarily made up of collagen fibers and keratocytes, which are irregularly shaped corneal cells responsible for producing crystallin to maintain the optical properties of the cornea, such as transparency and refractive performance [24]. The density of keratocytes is high at the anterior side of the stroma and decreases towards the posterior side [25, 26]. The collagen fibers and keratocytes form layers structured like the pages of a book, and approximately 200 such layers exist in a healthy adult human. The pre-Descemet's layer (PDL), or Dua's layer, named after the person who discovered it in 2013 [27], is often considered the last portion of the stroma. PDL is a transparent region that contains types of collagen but no keratocytes. Due to its thinness, only one research group has successfully imaged this layer in vivo in humans to date [28]. Descemet's membrane, also known as the posterior limiting membrane, follows the stroma (adjacent to the PDL). It is a primarily collagen-based layer that serves to separate the stroma from the endothelium, with an average thickness of 5 to 20 μm, depending on the age of the subject [27-29]. The endothelium is the final layer of the cornea and is a single-cell-layer structure with a thickness of approximately 5 μm. It acts as a barrier to the anterior chamber of the eye while allowing the exchange of fluids and solutes between the stroma and aqueous humor [30]. The endothelial cells are hexagonal shaped with an average diameter of 20 μm in healthy adults. The density of endothelial cells tends to decrease with age [23, 28, 31].

1.3 Thesis Organizations

This thesis is structured based on three journal articles which are either published, under review, or awaiting submission. The detailed contributions of the thesis author to each article are listed in the 'Statement of Contributions' section of the thesis. Here is the breakdown of the thesis chapter contents:

Chapter 2 briefly reviews the principle of OCT with low coherence interferometry, compares the differences between Time-Domain OCT and Fourier-Domain OCT, reviews different OCT scanning approaches, and presents the characteristics of Fourier-Domain OCT. Additionally, the concept of dynamic OCT is briefly discussed at the end of the chapter.

Chapter 3 focuses on the development of a Powell lens-based line-scan OCT system, followed by the system performance characterizations and the presentation of ex-vivo biological tissue imaging results.

Chapter 4 is dedicated to the development of the second-generation Powell lens-based line-scan OCT system and presents the in-vivo human cornea imaging results.

Chapter 5 describes the development of a line-scan OCT system and a dynamic OCT data processing algorithm for dynamic OCT studies. It also shows the results generated from ex-vivo biological tissue using dynamic OCT.

Chapter 6 summarizes the work completed during the MSc study and briefly discusses future work.

Chapter 2
An Introduction to Optical Coherence Tomography (OCT)

Optical Coherence Tomography (OCT) is often considered the optical equivalent of ultrasound imaging. It enables non-invasive, cross-sectional imaging of biological tissues with cellular resolution through a low-coherence interferometry technique [1]. Since its invention in 1991, OCT has been widely used for various imaging applications in ophthalmology and beyond. This is particularly true following the development of Fourier Domain OCT (FD-OCT), which significantly improved data acquisition speed and system sensitivity compared with Time Domain OCT (TD-OCT) [32-34]. To help understand the basic OCT image terminology, as well as the typical OCT imaging outcomes, Fig. 2.1 shows healthy human cornea data displayed in gray-scale with logarithmic operation applied to the raw OCT data to enhance visibility, which will be discussed in detail in Chapter 4. Starting from the left is an A-scan, a 1D intensity array in the axial direction (Z-direction), which is considered the fundamental structure of an OCT image (Fig. 2.1 left). Combining multiple A-scans taken at different locations can form a 2D image (XZ Intensity image), also called a B-scan image (Fig. 2.1 middle). Similarly, combining multiple B-scans taken at different locations can assemble a 3D image set, known as a Volume-scan image (Fig. 2.1 right).

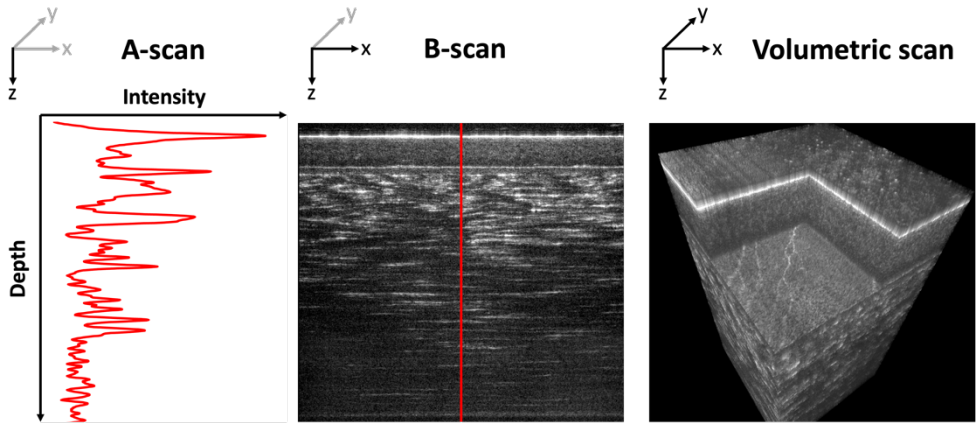

Fig. 2.1. A-scan (left), B-scan (middle) and volumetric scan (right) of human cornea.

This chapter briefly reviews the basic principles of OCT with low coherence interferometry, characterizes different OCT imaging modalities as well as OCT techniques utilized in this MSc study.

2.1 OCT with Low coherence interferometry

Figure 2.2 shows a free space OCT system schematic design based on a Michelson interferometer. Assume that the low coherence light source generates a propagating electromagnetic field, with electric field component characterized by the equation $E_i = s(k)e^{i(kz-\omega t)}$. Here $s(k)$ describes the amplitude of the electric field in terms of wavenumber k. The magnetic field component is ignored as it does not contribute to OCT imaging. The beam splitter (here we assume a perfect 50:50 beam splitter) splits the light into the reference arm that ends with a reflection mirror and the sample arm that ends with a multi-layer sample. The light reflected from the mirror and the multi-layer sample are respectively characterized by the equations $E_R = \frac{E_i}{\sqrt{2}} r_R e^{i2kZ_r}$ and $E_s = \frac{E_i}{\sqrt{2}} [r_s(Z_s)] \otimes e^{i2kZ_s}$. Here Z_r is the distance from the beam splitter to the reflective surface in the reference arm, and Z_s represents the distance from the beam splitter to the reflective layers within the sample arm. r_R is the electric field reflectivity of the reference mirror and $r_s(Z_s)$ is the electric field reflectivity of the multi-layer sample as a function of individual sample layers. Assuming n discrete sample layers, $r_s(Z_s) = \sum_{i=1}^{n} r_{s,i}\delta(Z_s - Z_{s,i})$, where $r_{s,i}$ is the reflectivity of the i-th layer at depth $Z_{s,i}$, and δ represents the Dirac delta function indicating the location of each layer.

The signals from two arms are collected by the detector. The generated detector photocurrent follows the expression:

$$I(k) = \frac{\rho(k)}{2}\langle |E_R + E_s|^2 \rangle = \frac{\rho(k)}{2}\langle (E_R + E_s)(E_R + E_s)^* \rangle \quad (2.1)$$

Here $\rho(k)$ is the responsivity of the detector and the angle brackets indicate the response time of the detector. Expanding Equation (2.1) with the E_R and E_s expressions described earlier, and keeping the real part of the result gives:

$$I(k) = S(k)\left\{ r_R^2 + \sum_{i=1}^{n} r_{s,i}^2 + 2\sum_{i=1}^{n} \sqrt{r_R r_{s,i}} \cos\left[2k(Z_r - Z_{s,i})\right] + \sum_{i,j=1, i\neq j}^{n} \sqrt{r_{s,i} r_{s,j}} \cos\left[2k(Z_{s,i} - Z_{s,j})\right] \right\} \quad (2.2)$$

Here $S(k) = \frac{\rho}{4}\langle s(k)^2 \rangle$. The first two terms r_R^2 and $\sum_{i=1}^{n} r_{s,i}^2$ are the constant or 'DC' terms, referring the direct reflections from the reference mirror and sample layers, without interference occurring. The r_R^2 term can be characterized before imaging and subtracted from the final result. The $\sum_{i=1}^{n} r_{s,i}^2$ term is normally negligible since the electric field reflectivity of the sample layers is much smaller than that of

the reference mirror. The term $2\sum_{i=1}^{n}\sqrt{r_R r_{s,i}}\cos\left[2k(Z_r - Z_{s,i})\right]$ is the 'cross-correlation' term, corresponding to the interference signals from sample layers and the reference mirror. This is the term that OCT relies on to extract low coherence interferometry amplified signals. The last term $\sum_{i,j=1,i\neq j}^{n}\sqrt{r_{s,i}r_{s,j}}\cos\left[2k(Z_{s,i} - Z_{s,j})\right]$ is the 'auto-correlation' term that is associated with interference signals that occur within different sample layers. This term is also generally negligible due to the low electric field reflectivity of the sample layers. The differences between TD-OCT and FD-OCT, which will be discussed in more detail in Section 2.2, arise from different interpretations of Equation (2.2).

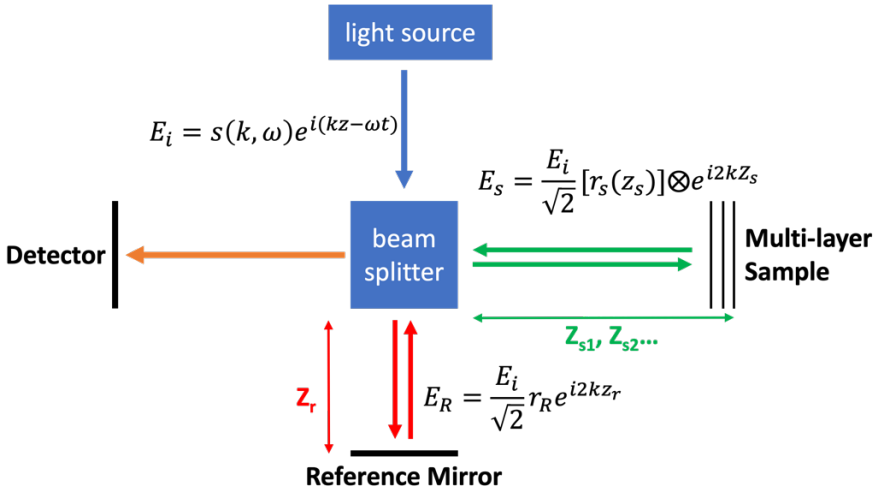

Fig. 2.2. Free space OCT set up with Michelson interferometer design. $\boldsymbol{s(k)}$ is the amplitude of the incident electric field in terms of wave number $\boldsymbol{k}$. $\boldsymbol{r_R}$ and $\boldsymbol{r_s(Z_s)}$ are the electric field reflectivity of the reference mirror and sample layers. $\boldsymbol{Z_r}$ and $\boldsymbol{Z_s}$ are the path length from the beam splitter to reflection surfaces in the reference and sample arms respectively.

2.2 Time Domain OCT and Fourier Domain OCT

Assume the incident light has a Gaussian wave profile with $s(k) \propto e^{-\left(\frac{k-k_0}{\Delta k}\right)^2}$ where k_0 is the central wavenumber and Δk is half-width of the spectrum at $1/e$ intensity of its maximum. Taking the integral of Equation (2.2), the cross-correlation term with respect to all wavenumbers gives:

$$I_{cc}(z_R) = \int_0^\infty I_{cc}(k)dk \propto \sum_{i=1}^{n}\sqrt{r_R r_{s,i}}e^{-(Z_r - Z_{s,i})^2\Delta k^2}\cos\left[2k_0(Z_r - Z_{s,i})\right] \quad (2.3)$$

The $e^{-(Z_R - Z_{s,i})^2 \Delta k^2}$ term suggests that the interference signal will peak at $Z_r = Z_{s,i}$ and quickly diverge with the increment of path length difference. The width of the interference signal is determined by the Fourier transform of $s(k)$. This will be discussed further in Section 2.4.1. One method to generate information along the A-scan direction is to adjust the reference path length Z_r to match various sample path lengths, or $Z_{s,i}$ values, with a linear stage to translate the reflection mirror, a piezoelectric actuator-based fiber stretcher, or other methods. This OCT imaging modality is called Time Domain OCT (TD-OCT). Conventionally, TD-OCT achieves an A-scan rate on the order of a few kHz, which is limited both by the performance of the moving mechanical components such as galvo scanners and fiber stretcher and by Signal-to-Noise Ratio (SNR) considerations due to reduced exposure time. Figure 2.3(A) shows a TD-OCT system schematic; by using a translational reference mirror, information from different depths can be collected.

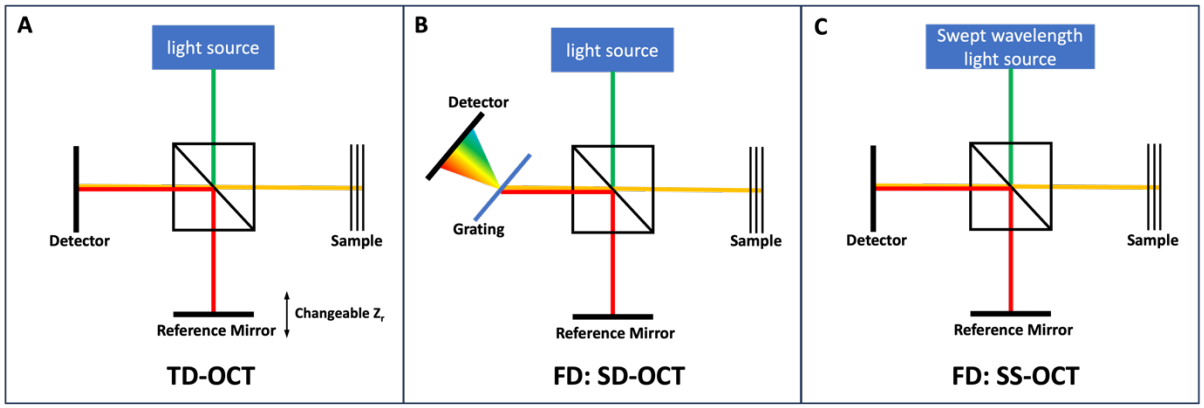

Fig. 2.3. Schematic of different OCT systems. (A) TD-OCT. (B) Type one of FD OCT: SD-OCT and (C) Type two of the FD-OCT: SS-OCT.

An alternative to TD-OCT is FD-OCT, which offers data acquisition speeds that are orders of magnitude faster and provides a higher system SNR compared to TD-OCT. In FD-OCT, a Fourier transform is applied to the cross-correlation term in Equation (2.2) instead of an integral with respect to wavenumbers. This yields:

$$I_{cc}(z) = \mathcal{F}\{I_{cc}(k)\} \propto \gamma(z) \otimes \sum_{i=1}^{n} \sqrt{r_R r_{s,i}} \{\delta\left[\left(z \pm 2\left(z_r - z_{s,i}\right)\right)\right]\} \quad (2.4)$$

Here, $\mathcal{F}\{I_{cc}(k)\}$ represents the Fourier transform of the k-space cross-correlation term. $\gamma(z)$ is the Fourier transform of $s(k)$, which is the coherence function. Simplifying Equation (2.4) further by computing the convolution yields:

$$I_{cc}(z) \propto \sum_{i=1}^{n} \sqrt{r_R r_{s,i}} \{\gamma\left[2\left(z_r - z_{s,i}\right)\right] + \gamma\left[-2\left(z_r - z_{s,i}\right)\right]\} \quad (2.5)$$

Equation (2.5) contains information from all discrete layers within the scanning range to form an A-scan, eliminating the need for mechanical components to change the optical path. The two terms $\gamma\left[2\left(z_r - z_{s,i}\right)\right]$ and $\gamma\left[-2\left(z_r - z_{s,i}\right)\right]$ differ only in sign and arise from the mirror artifact of the Fourier transform. FD-OCT requires a resolved interference k spectrum to carry out the Fourier transform computation. This is typically achieved by adding a grating in front of the camera to separate the continue emission (CW) broadband light into different wavelengths, or by using a tunable swept wavelength/ frequency light source to quickly sweep a very narrow band of the spectrum over time. Both approaches fall under the FD-OCT category and are respectively named Spectral Domain OCT (SD-OCT) and Swept-Source OCT (SS-OCT) for clearer distinction. Figures 2.3(B) and 2.3(C) show the schematic diagrams of an SD-OCT system and an SS-OCT system, respectively.

2.3 OCT imaging modalities

OCT can be characterized into three main categories of scanning approach: point-scan OCT (PS-OCT), line-scan OCT (LS-OCT) and full-field OCT (FF-OCT). Fig. 2.4 presents a diagram that illustrates the three imaging modalities and their differences in beam shapes on the image plane. For the sake of simplicity and consistency, we assume that all systems employ a microscopic objective (indicated by the gray blocks in the diagram) to manipulate light before the image plane. Although the TD-OCT approach is applicable to all three modalities, this discussion centers on the FD-OCT approach, which has been the most prevalently used in the field in recent decades and is the method employed in this thesis.

PS-OCT systems project a focused pencil beam onto the sample. The depth information relative to the point is encoded within the spectrum. A single camera exposure (for SD-OCT) or one full spectrum sweep (for SS-OCT) generates an A-scan. To obtain a volumetric dataset, two linear scanning scanners or micro-electromechanical system (MEMS) mirrors are used to translate the beam across the XY plane. The ability to control the focusing beam with two degrees of freedom on the XY plane enables not only raster scans but also other scanning patterns, such as circular scans, which can be beneficial

for functional OCT studies. Since A-scans within the image volume are collected separately during data acquisition, there is no crosstalk between A-scans and better-quality images are generated with PS-OCT compared to other OCT imaging modalities with similar system SNR. However, because each A-scan exposure takes a certain amount of time, PS-OCT systems generally offer slower data acquisition speeds compared to LS-OCT and FF-OCT systems. Most commercial and clinical PS-OCT systems have an A-scan rate below 300 kHz. This can be challenging for large Field-of-View (FOV) volumetric imaging, as involuntary body movements and eye motions may introduce artifacts during data acquisition. With high-speed line cameras or special light sources such as Fourier domain mode-locked (FDML) lasers, researchers have reported A-scan rates of 600 kHz for a SD-PS-OCT system and 5.2 MHz for a SS-PS-OCT system [35, 36]. However, the SNR of the SD-PS-OCT system is limited by the short A-scan exposure time, and the axial resolution of the SS-PS-OCT system is limited by the swept source light source.

LS-OCT, or sometimes also called line-field OCT (LF-OCT), was first reported in 1999 [37]. It utilizes a 2D lens, often a cylindrical lens, to convert the circular-shaped beam into a line-shaped beam. This allows for the parallel collection of all data points along the line with a 2D sensor camera (for SD-OCT) or a line camera (for SS-OCT). One line-scan exposure directly generates one B-scan, enabling a significant improvement in data acquisition speed compared to PS-OCT systems. LS-OCT systems reported in the last decade could easily achieve MHz-equivalent A-scan rates with high enough system SNR for biological tissue imaging [12-14, 38-40]. For LS-OCT systems, acquiring volumetric scans requires only one linear scanner to translate the beam. Since the generation of a single B-scan frame does not require any mechanical movement in the system, LS-OCT B-scans normally offer better phase stability compared to other OCT imaging modalities. Despite the fast acquisition speed, LS-OCT systems do have limitations. For example, as shown in the middle diagram of Fig. 2.4, the LS-OCT incident beam lacks a confocal parameter in the line direction, which leads to more crosstalk between A-scans within a B-scan and a degradation in image quality. Furthermore, since the single-shot camera exposure time is normally longer for LS-OCT systems compared to PS-OCT systems, the motion induced interference fringe washout is a larger issue for in vivo imaging with an LS-OCT system. Finally, most LS systems use a cylindrical lens as the line generator, which leads to a line-shaped beam with a Gaussian intensity distribution along the line direction. The uneven intensity distribution can result in more than a 10 Decibel (dB) SNR variation along the line-direction FOV. One of the purposes of this MSc study is to utilize a 2D lens with a conically shaped surface, called a Powell lens, to replace

the cylindrical lens as the line generator. This leads to a more uniform line-direction SNR distribution. More details on the Powell lens-based LS-OCT research are discussed in Chapters 3 and 4, respectively.

FF-OCT is another type of parallel data acquisition OCT modality that was first reported in 2006 [41]. Unlike LS-OCT, which acquires a B-scan image with a single camera exposure, FF-OCT acquires an enface (XY plane) image with one single camera exposure by projecting a parallel beam onto the sample, as shown in the right diagram of Fig. 2.4. Since the projected beam already contains 2D information, the SD method is not a viable option for FF-OCT, that would require a 3D camera sensor to collect both 2D image and 1D spectrum information. Consequently, FF-OCT systems utilize either TD or SS approaches to generate volumetric images. Because the incident beam on the image plane is a parallel beam, a major advantage of FF-OCT is that it is not constrained by the depth of focus (DOF) due to beam focusing, allowing the use of high-numerical-aperture (NA) objectives to achieve cellular-level lateral resolution throughout the entire scanning depth. However, conversely, the lack of a confocal parameter in any direction makes crosstalk a serious issue for FF-OCT systems.

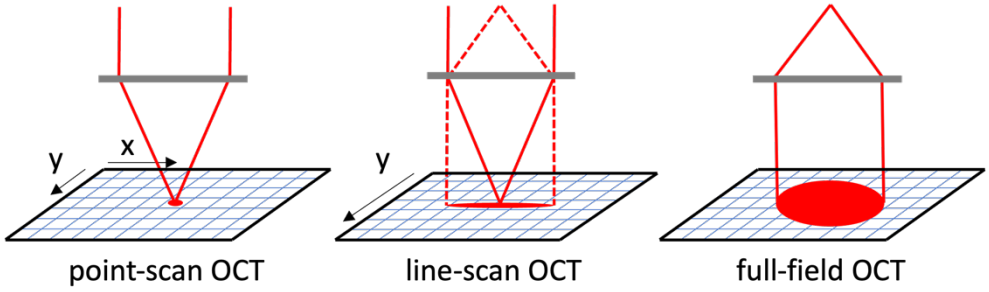

Fig. 2.4. Beam shapes of point-scan OCT, line-scan OCT, and full-field OCT on the image plane.

2.4 Fourier Domain OCT characteristics

This section describes some OCT characteristics related to this study. Unless specified otherwise, all the characteristics mentioned in this section are based on the PS-OCT system setup. Assume a normalized Gaussian intensity input beam profile with electric field amplitude $s(k) = \frac{1}{\Delta k\sqrt{\pi}} e^{-\left(\frac{k-k_0}{\Delta k}\right)^2}$.

2.4.1 Axial resolution

OCT axial resolution describes the system's theoretical limit to resolve two distinct points in the axial direction for a given OCT system. Unlike many other characteristics, axial resolution is independent of

the system's physical setup and is only related to the input light profile. The Fourier transform of $s(k)$ yields the coherence function:

$$\gamma(z) = \mathcal{F}\{s(k)\} = e^{-z^2 \Delta k} \quad (2.6)$$

The axial resolution (δ_z), also defined as the coherence length (l_c) of light, is typically characterized by the Full-Width-at-Half-Maximum (FWHM) of the coherence function:

$$\delta_z = l_c = \frac{2\sqrt{\ln(2)}}{\Delta k} = \frac{2\ln(2)}{\pi}\frac{\lambda_0^2}{\Delta\lambda} \quad (2.7)$$

Here, $\lambda_0 = \frac{2\pi}{k_0}$ represents the central wavelength of the spectrum and $\Delta\lambda$ is the FWHM spectrum width. In practice, for non-Gaussian intensity beam profiles, Equation (2.7) should be used only as a rough estimation of the finest limit of the light's coherence length. Instead, the axial resolution should be calculated by taking the Fourier transform of the actual beam profile.

2.4.2 Lateral resolution

The theoretical lateral resolution (δ_x) of an OCT system can be characterized as the light propagates through a confocal microscope, where the light power distribution $I(v)$ at the focal plane can be modeled as follows:

$$I(v) = \left(\frac{2J_1(v)}{v}\right)^4 \quad (2.8)$$

Here, $J_1(v)$ is the first-order Bessel function of the first kind, and v is the normalized lateral parameter, defined as $v = \frac{2\pi x sin(\alpha)}{\lambda_0}$. In this expression, x represents the lateral distance away from the light propagating axis, and $\sin(\alpha)$ is the NA of the microscopic objective, assumed to be filled properly. The lateral resolution is defined as the FWHM of the intensity diameter of the beam width at the focal plane, and is given by the following equation:

$$\delta_x = \frac{\sqrt{2\ln(2)}}{\pi}\frac{\lambda_0}{\sin(\alpha)} \approx 0.37\frac{\lambda_0}{\sin(\alpha)} = 0.37\frac{\lambda_0}{NA} \quad (2.9)$$

One point to note is that Equation (2.9) involves only a single wavelength, λ_0, which suggests that the lateral resolution is dependent on a specific wavelength. For a narrow-band input spectrum, the calculation based on the spectral central wavelength can provide a reasonable approximation of the system's lateral resolution. However, this is not the case for a broadband spectrum input.

2.4.3 Depth of Focus

Assuming a propagating Gaussian beam with intensity profile:

$$I(r) = I_0 e^{-\frac{2r^2}{w(z)^2}} \quad (2.10)$$

Here, z is the propagating axis, r is the radial distance away from the propagating axis and $w(z)$ is the radius of the beam with $1/e^2$ beam intensity relative to I_0 at a given plane z. When the light is at the focal plane, i.e. the $w(z = 0)$ plane, the $1/e^2$ beam radius is called the beam waist of the Gaussian beam, denoted as w_0 and given by $w_0 = \frac{\lambda_0}{\pi NA}$. The Rayleigh length, or Rayleigh range, Z_R describes the axial distance from the beam waist such that $w(z) = \sqrt{2}w_0$, and is given by $Z_R = \frac{\pi w_0^2}{\lambda_0} = \frac{1}{\pi}\frac{\lambda_0}{NA^2}$. The DOF, also called the confocal parameter b, is defined as twice the Rayleigh range and is given by:

$$DOF = b = 2Z_R = \frac{2\pi w_0^2}{\lambda_0} = \frac{2\lambda_0}{\pi NA^2} \quad (2.11)$$

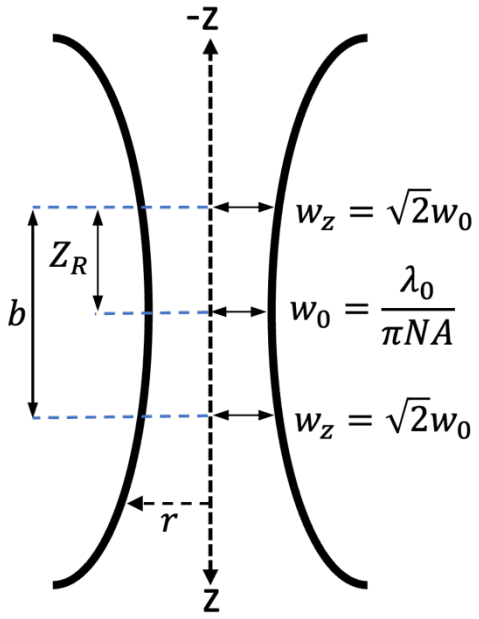

Fig. 2.5. Diagram of a Gaussian beam near the focal plane.

2.4.4 Scanning range

Based on Equation (2.2), the auto-correlation term of the OCT interference fringe presents as a sinusoidal function of the form $\cos[2k(z_r - z_{s,i})]$. With a larger difference in optical path length, the interference fringe will exhibit a higher frequency. For a detector with a finite number of pixels, the maximum frequency that can be detected is governed by the Nyquist-Shannon sampling theorem. Mathematically, for a detector with N pixels, and a broadband light source with spectrum width Δk, the inequality $2\Delta k(z_r - z_{s,i}) \leq \frac{N}{2} \times 2\pi$ should be satisfied to prevent aliasing. The maximum scanning range, Z_{max}, can then be determined by setting both sides of the inequality equal, which yields:

$$2(\mathrm{k_{max}} - k_{\mathrm{min}})Z_{max} = N\pi \quad (2.12)$$

Re-arranging Equation (2.12) to isolate Z_{max} gives:

$$Z_{max} = \frac{N\pi}{2(k_{max} - k_{\mathrm{min}})} = \frac{N}{4(\frac{1}{\lambda_{min}} - \frac{1}{\lambda_{max}})} \quad (2.13)$$

2.4.5 Digital resolution

The digital resolution $\tilde{\delta}$ of an OCT system is defined as the ratio between the FOV and the number of pixels that cover the FOV. Since the axial and lateral resolutions of an OCT are quantified separately, their respective digital resolutions are also defined separately, as follows:

$$\widetilde{\delta_x} = \frac{FOV_x}{N_x} \quad (2.14)$$

$$\widetilde{\delta_z} = \frac{Z_{max}}{N/2} = \frac{1}{2(\frac{1}{\lambda_{min}} - \frac{1}{\lambda_{max}})} \quad (2.15)$$

Here, $\widetilde{\delta_x}$ and $\tilde{\delta}_z$ represent the digital resolutions in lateral and axial directions, respectively. In Equation (2.14), FOV_x is the field of view in the X direction and N_x is the total number of pixels, or A-scans in the X direction. The Y direction is described by the same expression. For Equation (2.15), N is the total number of camera pixels used for spectral collection. The factor of $1/2$ in the denominator is indicative of a mirror artifact arising from the Fourier transform. To prevent aliasing, the digital resolution of the system should be at least half of the actual resolution, in accordance with the Nyquist-Shannon sampling theorem.

2.4.6 Signal-to-Noise Ratio

For OCT, the system's SNR is defined as:

$$SNR = \frac{\langle I_D \rangle^2}{\sigma^2} \quad (2.16)$$

which is the ratio of the mean-square peak signal power, $\langle I_D \rangle^2$, on the detector to the noise variance, σ^2. Based on Equation (2.2), if only the signal at $z_R = z_s$ is considered, then the cross-correlation intensity can be expressed as:

$$I_{cc} = \rho(k) s^2(k) \sqrt{r_R r_s} \quad (2.17)$$

Given a specific camera integration time τ, and camera quantum efficiency η, Equation (2.17) can be modified as follows:

$$I_D = \frac{\eta \tau}{h\nu} s^2(k) \sqrt{r_R r_s} \quad (2.18)$$

Here, h is the Planck's constant and ν is the photon frequency of photons. Assuming the shot-noise-limit condition, the noise on the detector is dominated by the direct reflection from the reference arm and the noise variance follows the Poisson distribution as:

$$\sigma^2 = s^2(k) r_R \frac{\eta \tau}{h\nu} \quad (2.19)$$

Combining Equations (2.16), (2.18) and (2.19) yields:

$$SNR = \frac{\eta \tau}{h\nu} s^2(k) r_s = \frac{\eta \tau P_s}{h\nu} \quad (2.20)$$

Equation (2.20) describes the OCT SNR assuming a perfect detector for the interference fringes. However, as briefly mentioned in Section 2.4.4, the interference fringe frequency is a depth-dependent quantity. According to the Nyquist-Shannon sampling theorem, a higher-frequency fringe may be less effectively differentiated by a detector with a finite number of pixels, leading to a drop in SNR. This phenomenon is known as SNR roll-off [42]. It is also important to note that although the terms "SNR" and "sensitivity" can be defined differently under various scenarios, for the purposes of this thesis, the two terms are used interchangeably.

2.5 Dynamic OCT

Dynamic OCT (dOCT) extends conventional OCT by utilizing temporal variations in the OCT signal, which are measured by taking multiple exposures at the same location at different times, to provide

contrasts in morphological images. This technique enables differentiation of tissues that appear homogeneous in standard images [35, 43], identification of cells with minimal intensity [44, 45], and facilitates the study of metabolic activities ranging from individual cells to cell clusters [46-49]. Additionally, it aids in the investigation of intracellular motions, among other applications [50-53]. Various analytical methods for intensity variation, such as time-dependent motility amplitude [54], intensity variance [48], signal correlation decay speed [49], mean frequency [55], and eigenvalue decomposition [56], are employed to extract the dOCT signal – each offering distinct advantages. The dOCT data collection system and the dOCT algorithm used in this thesis, as well as their various applications to biological tissues, will be discussed in detail in Chapters 5.

Chapter 3
Powell lens-based line-field optical coherence tomography system for cellular resolution imaging of biological tissues

3.1 Introduction

OCT technology can be classified in three categories, point-scanning, full field and line field, based on the scanning approach used for generation of volumetric images [1]. In point-scanning OCT (PS-OCT) a focused Gaussian beam is raster scanned in the transverse (XY) plane while simultaneously recording depth profiles (Z) for generation of a 3D image. Jitter from the mechanical scanning causes phase instability in the X and Y directions in the acquired imaging data. This phase instability can hinder the ability of OCT technology to measure accurately blood flow or functional responses of neural tissue to external stimulation and can cause motion artefacts in OCT images acquired with spatial resolution of ~ 1 μm. In Full Field OCT (FF-OCT), a wide optical beam is incident on the surface of the imaged object and scattered light from is projected onto the sensor of a 2D camera. Volumetric FF-OCT images are acquired by translating the focal plane in Z direction with simultaneous change of the optical pathlength in the reference arm of the system. Since there is no mechanical scanning in the XY plane, FF-OCT offers high phase stability in the transverse imaging plane [1,2]. In Line-Scan (LS) or Line-Field (LF) OCT, a line shaped beam is projected onto the surface of the imaged object and scanned in Y direction while data in Z direction is acquired simultaneously to form a volumetric image [3]. Therefore, LF-OCT offers high phase stability in the XZ plane with some scanning mirror jitter related phase instability in the Y scanning direction [4].

While the concept of LF-OCT was first proposed two decades ago [5], it took more than a decade for suitable fast, 2D camera technology to be developed. Over the past ~10 years multiple research groups have developed LF-OCT for structural [6], vascular [7,8] and functional [9–11] imaging of the human retina, cellular resolution imaging of the human cornea and limbus [12], as well as cellular resolution imaging of human skin [13–16].

Almost all LF-OCT systems that have been reported so far use a cylindrical lens as the line generator, which results in an elliptically shaped transverse profile of the beam with Gaussian intensity distribution along the major and minor axis of the ellipse. This leads to progressive loss of image contrast from the center of the line (B-scan width) to its edges. The typical quick solution to this problem adopted by

many research groups is to simply cut the low contrast areas of the acquired LF-OCT image. However, this approach is wasteful as it significantly reduces the image FOV. Expanding the line length by a factor of 4x or more and using only the central part of the Gaussian profile for imaging can reduce the loss of image contrast in cylindrical lens based LF-OCT systems. However, this approach has multiple drawbacks: a) waste > 50% of the optical power, which will require much more powerful light source to compensate for such a loss; b) require lenses with much larger focal lengths, that will increase the footprint of the LF-OCT system; c) parts of the laser line that are not used for imaging present a safety hazard for both the operator of the system and the imaged subject, therefore they need to be properly blocked, which may not be a trivial task. Digital compensation of the sensitivity loss is another option, though it will result in progressively higher noise level from the center to the edges of the FOV in the line direction.

An alternative approach is to replace the cylindrical lens with a Powell lens, which generates a top-hat light intensity profile in the line-direction. The Powell lens has been used as line a generator for numerous industrial applications for decades since its invention [17]. However, the first Powell lens-based LF-SD-OCT (PL-LF-SD-OCT) system was only reported recently [18]. While the design of this system is compact, simple and likely offers easy optical alignment, it has significant limitations in terms of spatial resolution and sensitivity. The authors used 15 mW optical power incident on the imaged biological tissue sample to achieve ~87 dB maximum sensitivity at an imaging rate of 3,500. This power exceeds the maximum permissible exposure (MPE) for ocular tissues as defined by the ANSI standard [19] by more than 3 times. Furthermore, the system has ~16 dB sensitivity roll-off and nearly 2× degradation of the FWHM of the axial PSF over a scanning range of ~ 850 μm (from ~2 μm near the zero-delay line to ~ 4 μm at 850 μm depth). Therefore, this design of the PL-LF-SD-OCT system may not be suitable for ophthalmic applications.

Here, a novel design of a PL-LF-SD-OCT system is presented, which offers ~2 μm × 2 μm × 1.8 μm (x × y × z) resolution in free space, ~87 dB maximum for 2.5 mW imaging power at 2,000 fps image acquisition rate. More importantly, the sensitivity loss in a single B-scan along the line direction is only ~1.6 dB. The system was validated by imaging plant tissue (cucumber) and animal cornea (rats).

3.2 Methods

3.2.1 Powell lens

Line generators such as cylindrical lenses and Powell lenses are designed to convert circularly shaped optical beams to line-shaped beams by restricting the propagation of light only in one of the transverse directions of the beam. Cylindrical lenses utilize a two-dimensional spherically shaped front surface, to bend the incident beam in one direction while leaving the orthogonal direction unchanged such that a line-shaped beam is formed. The line-shaped beam maintains Gaussian intensity distribution along the line direction (Fig. 3.1(A)–1(C)). In contrast, Powell lenses utilize a two-dimensional aspherical, conically shaped front surface, described with Equation (3.1):

$$z(r) = \frac{cr^2}{1+\sqrt{1-(1+k)(cr^2)}} \quad (3.1)$$

to generate a line-shaped beam with almost uniform intensity distribution along the line direction (Fig. 3.1(D)–1(F)) by introducing spherical aberrations in the original light profile [17, 20]. Here r is the radial distance from the light propagating axis, k is the conic parameter, and c is the radius of curvature of a sphere. Since the Powell lens does not have a focus, the concept of fan angle, which is the maximum expansion angle of the beam in the line direction, is used to characterize the lens. The back surface of the Powell lens can be either planar or curved, and its profile is used to control the fan angle size.

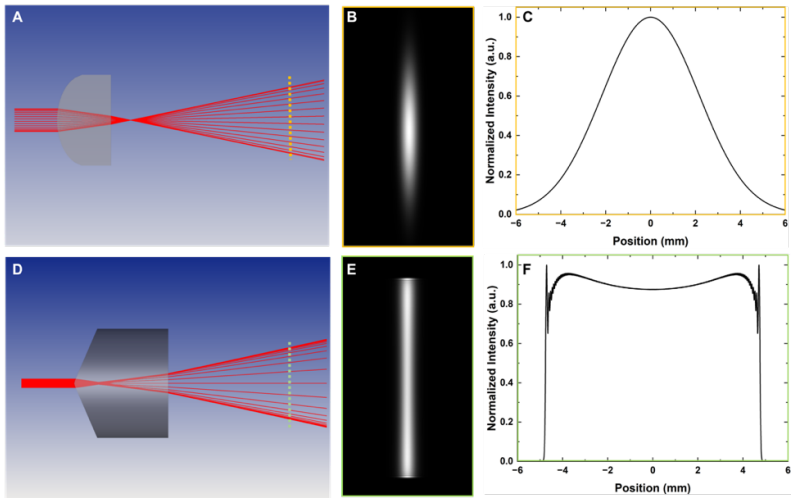

Fig. 3.1. Zemax simulations of beam propagation though a cylindrical lens (A) and a Powell lens (D). 1D and 2D cross-sectional light intensity distributions for the cylindrical (B and C) and Powell (E and F) lenses.

3.2.2 Layout of PL-LF-SD-OCT system

A schematic diagram of the PL-LF-SD-OCT system is shown in Fig. 3.2. The system is powered by a supercontinuum laser (SuperK Extreme, NKT Phonics). A custom filter unit (combination of long pass (600 nm cut-off), short pass (875 nm cut-off) and neutral density (ND) filters) is used to select a portion of the emission spectrum suitable for this study. A reflective collimator (RC04APC-P01, Thorlabs) is used to generate a collimated beam with 3.9 mm 1/e2 diameter and the measured output power directly after the collimator is ~12 mW. A Powell lens with 5° fan angle (Laserline Optics) is used to generate a line-shaped beam in the vertical (Y) direction. A telecentric pair of achromat doublets L1 (f = 75 mm) and L2 (f = 100 mm) is used to relay and magnify the beam. A non-polarizing beamsplitter (70:30 (R: T), BS023, Thorlabs) is used to split the incident beam between the sample and the reference arms of the Michelson interferometer. Multiple slits are used throughout the system to eliminate unwanted reflections from the optical components. In the sample arm of the system, the beam is focused (in Y direction) onto a 1D galvanometric scanner (GVS011, Thorlabs) to allow for acquisition of volumetric images. A telecentric pair of achromat doublets L3 (f = 80 mm) and L4 (f = 100 mm) is used to relay and magnify the beam in order to partially fill (~60%) the entrance aperture of a microscope objective (M Plan APO NIR 10×/0.26 NA, Mitutoyo). The optical power measured at the image plane is ~2.5 mW, which is below the maximum permissible exposure for human corneal and retinal tissue imaging as defined by the ANSI standard [19].

In the reference arm of the system, a cylindrical lens, CL1 (f = 75 mm) forms a telecentric pair with L2 in the vertical direction to convert the diverging line-shaped beam into an elliptically shaped parallel beam. Neutral density filters (NDF) are mounted along the optical path after CL1 to prevent saturation of the camera. A custom-built dispersion compensation unit (a pair of BK7 prisms) is used to compensate low orders of dispersion mismatch introduced by the optical components of the sample and reference arms (what we refer to as “hardware dispersion compensation”, or HDC). An iteration-based custom Python algorithm is used to numerically compensate dispersion mismatch with an approach similar to the one described in the Ref. [21]. An achromat doublet L5 (f = 30 mm) is used to focus the reference beam onto a mirror, mounted on a small translation stage. The mirror, L5 and the DC unit are mounted onto a large linear translation stage to control the optical path difference between two arms.

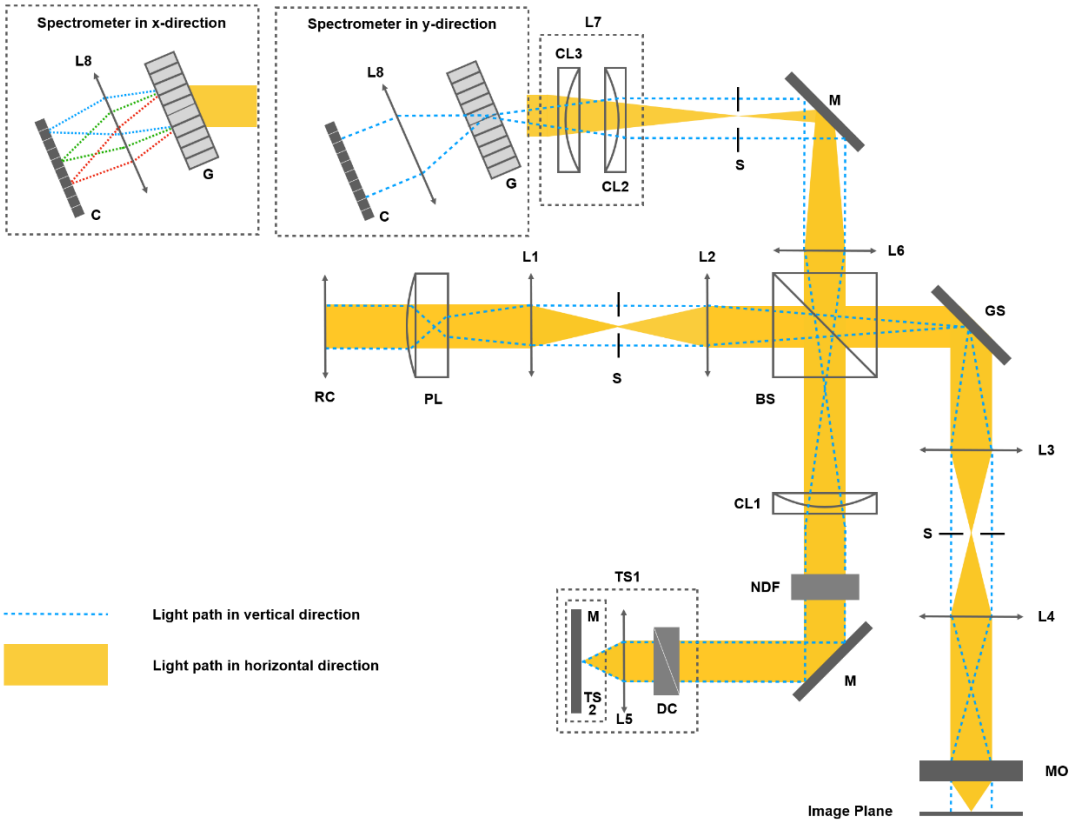

Fig. 3.2. A schematic diagram of the PL-LS-SD-OCT system. RC, reflective collimator; PL, Powell lens; L1-L6, achromatic doublets; BS, non-polarized beam splitter; CL, cylindrical lens; NDF, neutral density filter; TS, translation stage; DC, dispersion compensation unit; M, mirror; GS, galvanometric scanner; MO, microscopic objective; S, adjustable slit; G, transmissive grating; L8, camera lens; C, camera CMOS sensor. PL = 5° fan angle, L1 = 75 mm, L2=L4=100 mm, L3=80 mm, L5=30 mm, L6=200 mm, L8=85 mm, CL1=75 mm, CL2=150 mm, and CL3=250 mm.

In the detection arm of the system, a combination of lenses, L6 and L7 is used to relay the beam to the spectrometer. L6 is an achromat doublet (f = 200 mm), while L7 represents a pair of cylindrical lenses CL2 (f = 150 mm) and CL3 (f = 250 mm) with mutually orthogonal orientation, that are used to control the magnification of the beam separately in the X and Y direction [9,22]. The spectrometer is comprised of a volume phase holographic (VPH) transmission grating (990 l/mm @ 805 nm, Wasatch Photonics), and a camera lens (Planar T* 1.4/85, Zeiss). The transmitted optical beam is projected onto the sensor of a 2D CMOS camera (J-PRI, AOS technologies). The camera sensor has an area of 2,560 × 1,920 pixels, with a pixel size of 7.8 µm × 7.8 µm. For this design of the PL-LF-SD-OCT system, all

2,560 pixels were utilized in the spectral direction in order to achieve largest possible OCT scanning range. In the spatial (B-scan) direction, 600 pixels were used for volumetric image acquisition. The system's acquisition rate was set to 2,000 fps to achieve system sensitivity sufficient for imaging semi-transparent tissues such as cornea and retina. The maximum acquisition rate for the chosen region of interest (ROI) on the sensor (2,560 × 600 pixels) is 6,000 fps.

3.2.3 Data acquisition and processing

A custom LabVIEW-based algorithm was developed for data acquisition with the PL-LS-SD-OCT system. A set of custom Python-based algorithms were developed for processing of the raw data and generating dispersion compensated images. Amira (ThermoFisher Scientific) was used to render volumetric images and display enface projections from selected ROI.

3.3 Results

3.3.1 System performance

The performance of the PL-LF-SD-OCT system in terms of resolution and sensitivity was evaluated using either a protected silver mirror or a United States Air Force (USAF 1951) resolution target as the imaged object, and results from the tests are summarized in Fig. 3.3. The spectra measured separately at the detection arm of the system from mirror reflections in the reference and sample arms of the system are shown in Fig. 3.3(A). Note that the spectra were generated by averaging 50 consecutive frames to suppress the effect from the relative intensity noise (RIN) of the light source. The detected spectrum is centered at 730 nm with a FWHM spectral bandwidth of 135 nm. Figure 3.3(B) shows the system's axial point-spread function (PSF) measured at a depth of 100 μm relative to the zero-delay line after hardware dispersion compensation (HDC) only (black color) and after additional software dispersion compensation (SDC, red color). The PSF's FWHM is ~1.8 μm in free space, corresponding to ~1.3 μm in biological tissue assuming an averaged refractive index of 1.38. The system's axial resolution degrades slowly with depth, only by ~6% over 1 mm scanning range (Fig. 3.3(C)). The system's sensitivity was measured for ~2.5 mW incident optical power and 2,000 fps camera rate. As shown in Fig. 3.3(D), the median sensitivity measured at a depth of ~100 μm is ~87 dB with ~ 6 dB sensitivity roll-off over 700 μm and ~13 dB roll-off over the 1 mm scanning range. Figure 3.3(E) shows the sensitivity results for all 600 A-scans within a single B-scan, measured at a depth location of 100

μm away from the zero-delay line. These results show only ~1.6 dB loss of sensitivity from the highest peak of the B-scan to its edges.

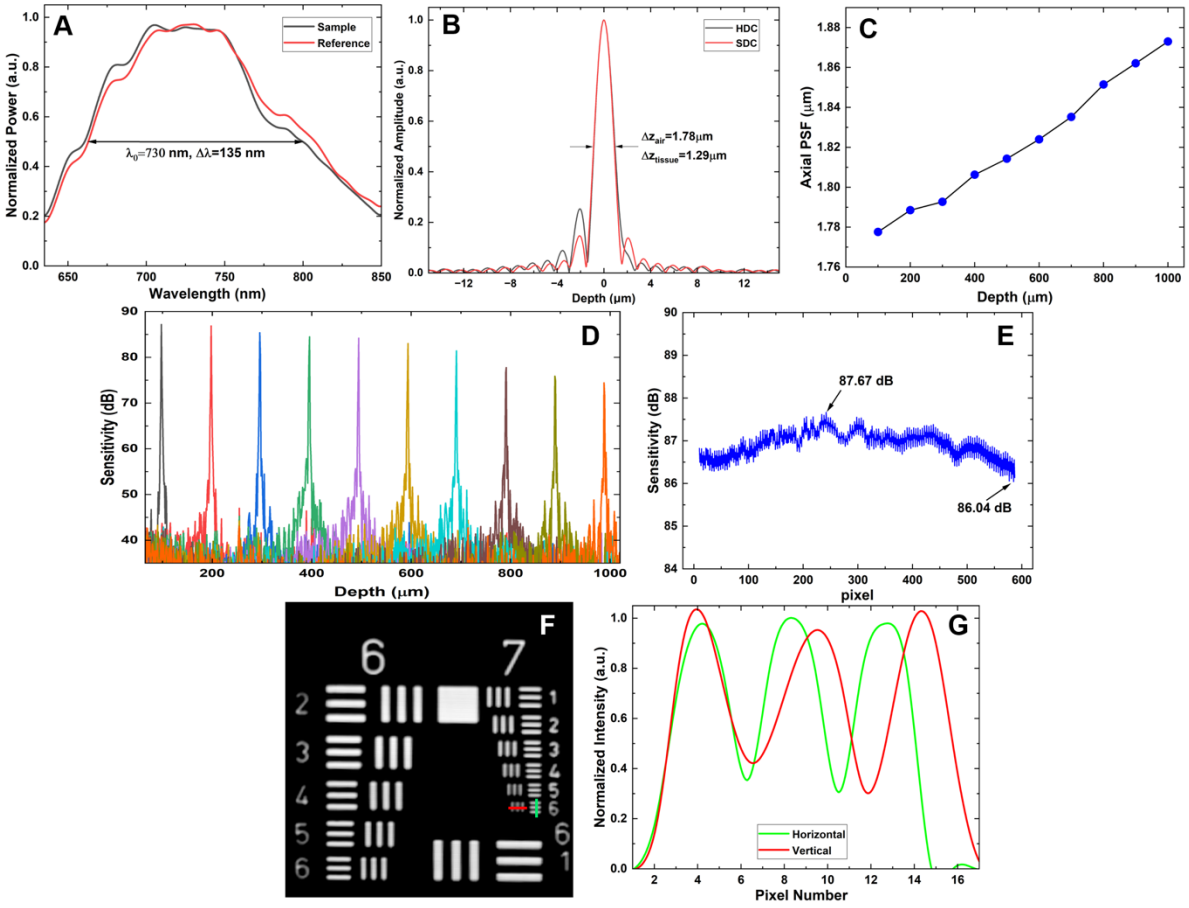

Fig. 3.3. (A) Spectra from the reference and sample arms measured at the detection end of the system. (B) Axial PSF measured at depth of 100 μm after HDC and HDC + SDC. (C) Depth-dependent degradation of the axial resolution. (D) Depth-dependent sensitivity. (E) Sensitivity distribution along the B-scan, measured at 100 μm depth. (F) Image of the USAF 1951 resolution target. (G) Normalized intensity profiles acquired from Group 7, Element 6 at the locations marked with the green and red lines in Fig. 3.3(F).

The system's lateral resolution and Field of View (FOV) were evaluated by imaging a USAF 1951 resolution target. With the current design of the system, the FOV is 263 μm (X) × 658 μm (Y), corresponding to 300 B-scans (X) and 600 A-scans in each B-scan (Y). Figure 3.3(F) shows an image of groups 6 and 7 of the resolution target. The intensity plots shown in Fig. 3.3(G) correspond to the

locations in Fig. 3.3(F) marked with the green and red lines. Since both the horizontal and vertical bars of group 7, element 6 can be clearly resolved and the width of 1 line of this element is equivalent to ~2.2 μm, therefore both the horizontal and vertical transverse resolution of the PL-LF-SD-OCT system are better than 2.2 μm.

3.3.2 Images of biological tissues

While the PL-LF-SD-OCT system is designed for imaging the human anterior eye segment (cornea and limbus), due to COVID-19 related restrictions on conducting clinical imaging studies, ethics clearance for use of the PL-LF-SD-OCT system for in-vivo imaging of the human anterior segment (cornea and limbus) has been delayed. Therefore, the performance of the system was evaluated by imaging plant tissue such as cucumber that has optical properties and cellular structure with size of the smallest cells similar to that of the human cornea, as well as imaging animal corneas (rats). For all imaging sessions, the optical power incident on the surface of the imaged object was 2.5 mW and the camera acquisition rate was set to 2,000 fps.

3.3.2.1 Cucumber

Figure 3.4 (A) shows a digital photograph of a transverse slice from cucumber. A magnified view (6×) of the ROI marked with the red square in Fig. 3.4(A) is shown in Fig. 3.4(B). The red arrow marks a cucumber seed with semi-transparent surrounding tissues. Figures 3.4 (C-H) were generated using Amira software. XZ, YZ and enface (XY) images of the cucumber seed and the surrounding tissue are shown in Fig. 3.4(C), 3.4(D) and 3.4E respectively, while Fig. 3.4(F) shows a volumetric image of the same region. Figures 3.3 (H) and 3.3 (G) show two enface images from the same 3D stack that correspond to different depths. Small cells of ~10 μm in size (Fig. 3.3 G, red arrow) located along the boundary of the cucumber seed (white arrow), as well as cellular nuclei in the larger cells are clearly resolved. Small reflective features were observed in the cytoplasm of larger cells (Fig. 3.3 H, green arrow), as well as double nuclei in one of the larger cells (Fig. 3.3 H, blue arrow).

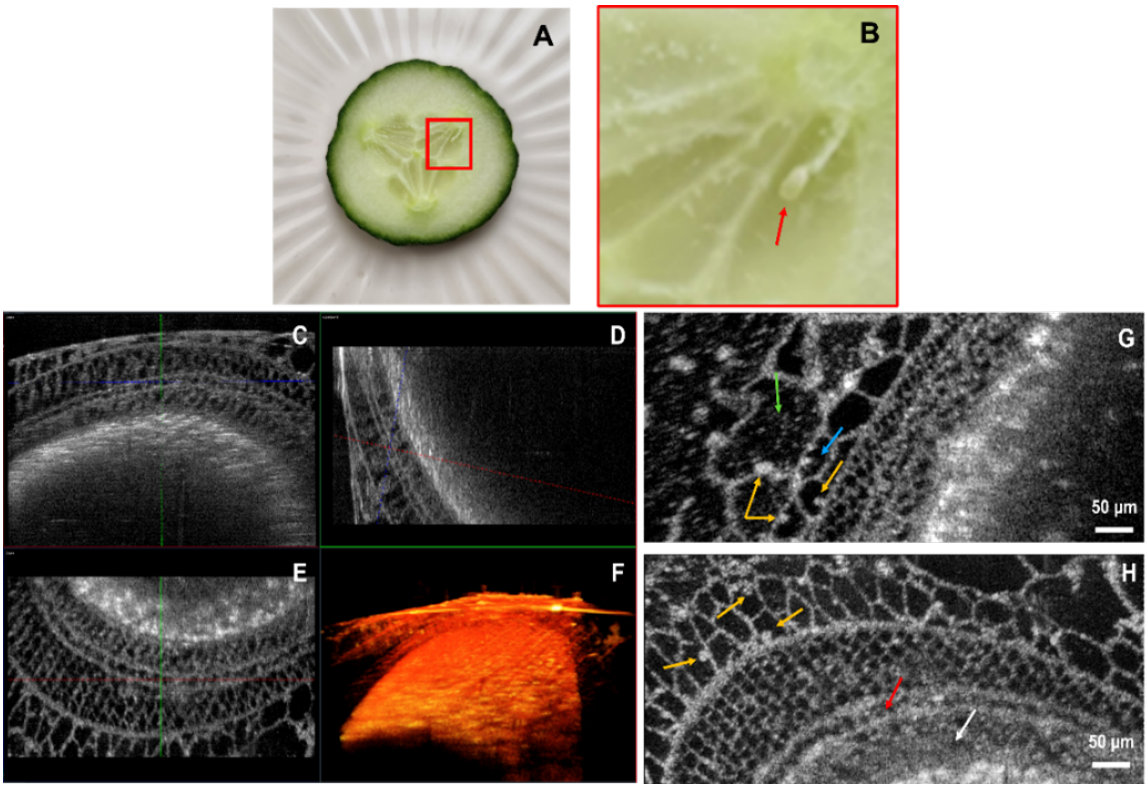

Fig. 3.4. Images of cucumber tissue. Digital photograph of transverse slide from cucumber (A). magnified view of the region of interest marked with the red square (B). PL-LS-SD-OCT images of the cucumber: XZ projection (C), YZ projection (D), enface projection (E), volumetric image (F), two enface projections corresponding to different depths (H and G). Cellular features are marked with colored arrows in Figs. 4 H and 4G: seed (white), small cells (red), cellular nuclei (orange), reflective features in the cytoplasm (green), cell with 2 nuclei (blue).

3.3.2.2 Rat cornea

The corneas of male Sprague-Dawley rats (~ 1 year old) were imaged with the PL-LF-SD-OCT system. All imaging sessions were conducted in compliance with the ethics regulations of the Office of Research Ethics, University of Waterloo. Immediately after euthanasia, rats were placed on a holder mounted on a XYZ translations stage as shown in the digital photograph in Fig. 3.5(A). A representative B-scan (XZ direction) of the rat cornea is shown in Fig. 3.5(B).

While all 5 of the major corneal layers (EPI – epithelium; BM – Bowman's membrane; STR – stroma; DM - Descemet's membrane; and END – endothelium) [23–25] are clearly resolved in the

image, many of these layers appear blurred. The blur is caused by the very short (~18 μm) depth-of-focus of the current design of the PL-LF-SD-OCT system. For the imaging data presented in Fig. 3.5 (B-D), the focal plane of the microscope objective was positioned at the anterior stroma to allow for imaging of keratocyte cells. The red arrow in Fig. 3.5(B) marks the Bowman's membrane, while the green arrow marks the basal cell layer in the corneal epithelium. Figures 3.5(C) and 3.5(D) show enface projections acquired from different locations the anterior and posterior stroma respectively. The yellow arrows mark stromal keratocytes, the blue arrow – thin corneal nerves in the anterior stroma, white arrow – larger stomal nerve located in the posterior stroma.

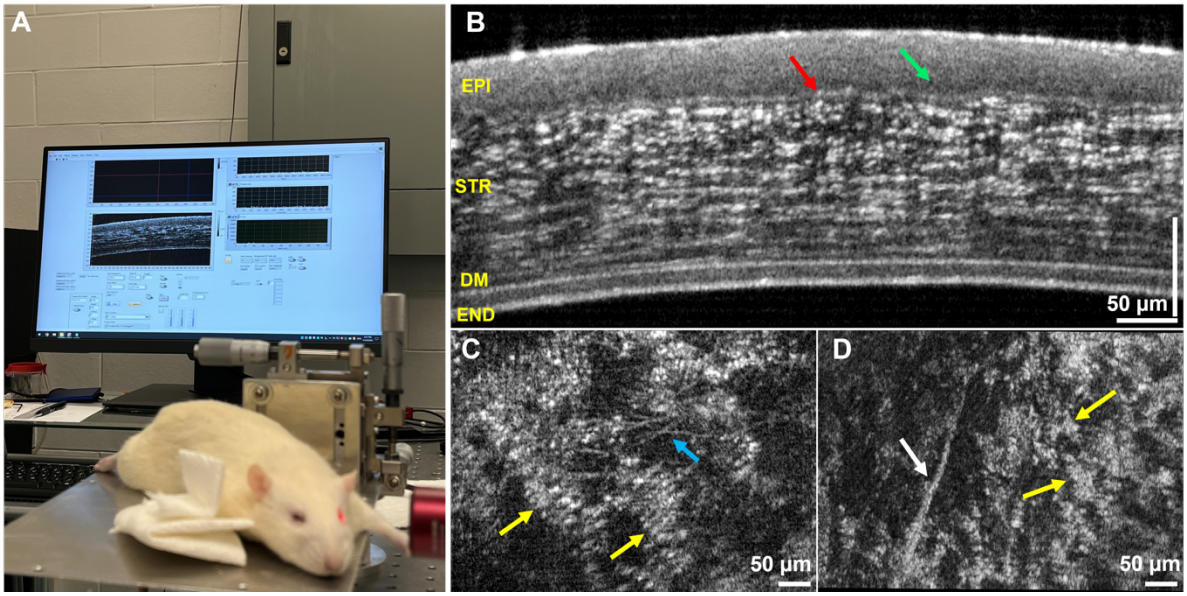

Fig. 3.5. (A) Digital photograph of the imaged animal. (B) Representative B-scan of the rat cornea (B) EPI -Epithelium; BM – Bowman's membrane; STR - Stroma; DM - Descemet's membrane; END - Endothelium; Red arrow: Bowman's layer, green arrow – basal cell layer of the epithelium. Enface projections acquired from the anterior (C) and posterior (D) stroma. Arrows mark: keratocytes (yellow); thin nerves in the anterior stroma (blue); thick nerve in the posterior stroma (white).

Cross-sectional and enface images of the posterior rat cornea that were acquired with the focal plane positioned at the endothelial layer are shown in Fig. 3.6. The cross-sectional images (Fig. 3.6(A) and 3.6(B)) were flattened and enface images of the endothelial layer (Fig. 3.6(C) and 3.6(D)) were generated using maximum intensity projection (MIP). The enface images (Fig. 3.6(C) and 3.6(D)) clearly show the honeycomb-like pattern of the endothelial cells, as well as dark, round spots inside the

cells that could correspond to cellular nuclei (red arrows) [12,25]. Line artefacts in the enface images (Fig. 3.6(D), blue arrow) are caused by the integer step-based flattening algorithm.

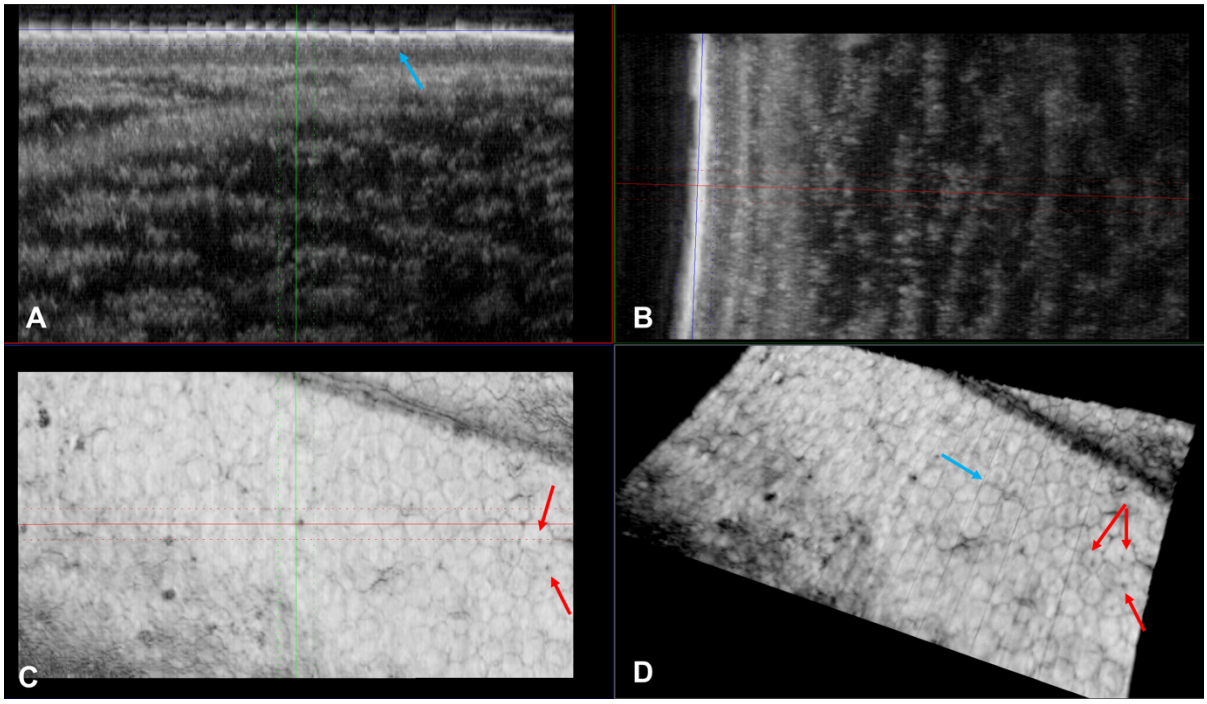

Fig. 3.6. Images of the corneal endothelium. XZ (A) and YZ (B) cross-sectional images of the posterior cornea showing the Descemet's membrane and the endothelium. Enface images of the endothelium (C) and (D) showing the cellular structure. Red arrows mark cellular nuclei, blue arrows mark artefacts generated by the integer-based flattening algorithm.

3.4 Discussion

The novel design of the PL-LF-SD-OCT system resulted in very high spatial resolution in biological tissue: ~2 µm isotropic lateral and ~ 1.3 µm axial (Fig. 3.3(B), 3.3 G and 3.3F), which was sufficient to visualize the cellular and sub-cellular structure of plant tissues (Fig. 3.4) and animal cornea (Fig. 3.5 and Fig. 3.6). Furthermore, the broadening of the axial PSF function over the entire scanning range (1 mm) was limited to only ~ 6% (Fig. 3.3(C)) compared to nearly 100% change reported by the Singaporean research group [18] over a scanning range of ~ 850 µm. Maximum sensitivity of 87 dB was achieved (Fig, 3.3D) for 2,000 fps image acquisition rate and 2.5 mW imaging power, which is well below the MPE recommended by the ANSI standard for in-vivo imaging of human ocular tissue. Given equal conditions (same frame rate and imaging power), the novel design proposed here offers an

improvement of ~ 5 dB in the maximum sensitivity measured close to the zero-delay line, compared to the design proposed by the Singaporean group [18]. A very important feature of the proposed novel design is the small (only ~ 1.6 dB) loss of sensitivity along the width of a B-scan (Fig. 3.3(E)), which is a very significant improvement compared to the sensitivity loss associated with LF-OCT systems based on cylindrical line generators (~10 dB or higher) [5–10,12–15]. Since the Singaporean research group [18] has not reported the B-scan sensitivity loss for their design, unfortunately, we cannot provide direct comparison between the 2 designs at this time.

In June 2022, our research group published a cylindrical lens-based design for a LF-SD-OCT system [12]. That design had two major limitations: a) Gaussian distribution of the optical power along the line, which resulted in ~ 10 dB loss of sensitivity from the center to the edges of the FOV along the line direction; and b) simplified design of the detection arm that did not allow for separate optimization of the transverse OCT resolution in the X and Y direction. The LF-SD-OCT system utilized a femtolaser (INTEGRAL, Femtolasers GmbH) with 3 dB spectral bandwidth of 130 nm, centered at 785 nm to achieve 1.7 μm axial and ~2 × 3 μm (X × Y) lateral resolution in biological tissue. The lower RIN of the femtolaser combined with the camera pixel size (11 μm × 11 μm) contributed to OCT system's sensitivity of ~92 dB measured near the zero-delay line for 2.6 mW optical power incident on the images object.

The PL-LF-SD-OCT system described here was designed to overcome some of the limitations of the LF-SD-OCT system. The substitution of the cylindrical lens with a Powell lens reduced the loss of sensitivity across the FOV from ~10 dB to ~1.5 dB. The use of supercontinuum laser with spectrum centered at ~730 nm and 3 dB spectral bandwidth of ~135 nm resulted in improvement of the axial OCT resolution in biological tissue from 1.7 μm to 1.3 μm. The addition of 2 cylindrical lenses (CL2 and CL3) in the detection arm of the PL-LF-SD-OCT system allowed for independent adjustment of the OCT lateral resolution in the X and Y direction.

While the current design of the novel PL-LF-SD-OCT system offers sufficiently high spatial resolution and sensitivity for imaging the cellular structure of semi-transparent biological tissues such as cucumber (Fig. 3.4) and rat cornea (Fig. 3.5 and Fig. 3.6), the design leaves plenty of room for improvement:

a) **Depth of focus** (DOF): The current design resulted in ~18 μm DOF, which is too short for imaging the cellular structure of the human cornea in one volumetric data set, as seen in Fig.

5(B). One approach to resolving this issue would be to trade lateral resolution for extended DOF by replacing the microscope objective in the current design with a lower magnification one. However, this approach is not desirable, as it will compromise the ability to visualize the cellular structure of corneal tissue, which was the main goal for designing the new PL-LF-SD-OCT system. An alternative approach would be to apply digital adaptive optics (DAO) [7,26–29] to correct for defocus and higher order aberrations in the PL-LF-SD-OCT images. We plan to utilize this approach in the near future.

b) **Sensitivity and sensitivity roll-off**: The current design offers maximum sensitivity of 87 dB near the zero-delay line with ∼13 dB sensitivity roll-off (Fig. 3.3(D)), which is sufficient for imaging the cellular structure of semi-transparent tissues such as the human and animal cornea, though will be problematic for imaging biological tissues that are more scattering such as skin. The sensitivity of the novel PL-LF-SD-OCT system is dependent on several factors: imaging power, image acquisition rate, efficiency of the optical design and RIN of the light source. Increasing safely the imaging power so that it is below the ANSI recommended MPE for ocular tissues is a very limited option, and in our case can result in only ∼1.5 dB sensitivity gain. Decreasing the camera acquisition rate to 1,000 fps will result in 3 dB sensitivity gain, however, this approach will introduce unwanted unvoluntary eye motion artefacts in the in-vivo human corneal images [8,30]. While the use of a broadband supercontinuum laser resulted in improvement of the PL-LF-SD-OCT axial resolution, the higher RIN noise of the laser in combination with the smaller pixel size (7.8 μm × 7.8 μm) of the AOS camera contributed to a slightly lower SNR (87 dB) measured near the zero-delay line with 2.5 mW imaging power. The use of low RIN light sources such as superluminescent diodes can further improve the SNR of the PL-LF-SD-OCT. The current optical design of the sample and detection arms of the PL-LF-SD-OCT system includes a large number of optical components that are lossy. Optimizing the efficiency of the collection of light scattered from the imaged object should improve the system's sensitivity. Furthermore, the smaller camera pixel size poses significant constraints on the optical design of the spectrometer and the PL-LF-SD-OCT system as a whole. The use of a camera with larger pixel size would improve the system's sensitivity, as well as the sensitivity roll-off, however, this approach will result in shorter scanning range for the same spectral range. Camera efficiency is another factor that contributes to the system's sensitivity. The use of cameras with

better quantum efficiency would improve the system's sensitivity and possibly the sensitivity roll-off.

c) **Powell lens**: While the use of a Powell lens greatly reduced the loss of sensitivity along the width of a B-scan compared to cylindrical lens-based LF-OCT systems, integration of the Powell lens in an OCT system is challenging. The Powell lens is a type of aspherical lens that does not have focus. The center of the optical beam incident on the lens needs to be precisely aligned with the conical tip in the transverse direction and must be coaxial with the central axis of the lens. Even small later shifts or tipping the beam relative to the axial direction results in non-uniform distribution of the optical power along the line length. As the Powell lens does not have a very well-defined focus, it is difficult to generate a collimated beam of the OCT system to allow for changes in the reference pathlength without significant loss of system's sensitivity due to misalignment between the refence and sample arm beams. In our case, this issue was resolved by use of a cylindrical lens in the reference arm to convert the line-shaped beam to an approximately circular and collimated beam in the reference arm of the system. Also, it should be noted that the quality of the Powell lens varies between manufacturers and imprecision in the Powell lens design can affect negatively both the resolution and the sensitivity of the PL-LF-SD-OCT system.

While only images of rodent cornea acquired postmortem were presented in this paper (Fig. 3.5 and Fig. 3.6), future biomedical applications of the novel PL-LF-SD-OCT system will focus on in-vivo imaging studies of the healthy and pathological human cornea and limbus. The design of the system can be adapted for retinal imaging by re-designing the sample arm of the PL-LF-SD-OCT system. By increasing the imaging power and decreasing the image acquisition rate, the current design of the system may also be suitable for imaging skin, as well as other highly scattering biological tissues and different biomedical applications.

3.5 Conclusion

A novel PL-LF-SD-OCT system that utilizes a Powell lens instead of cylindrical lens as the line generator was developed. This design resulted in significantly improved uniformity of the illumination along the line direction and only ~ 1.6 dB sensitivity loss between the B-scan's center and edges. The system's high spatial resolution allowed for imaging the cellular structure of plant tissues and the animal cornea, as well as resolving small morphological features such as cellular nuclei in the

endothelial cells. Future clinical applications of the PL-LS-SD-OCT system include in-vivo imaging of the healthy and pathological human cornea and limbus.

3.6 References

1. W. Drexler and J. G. Fujimoto, eds., Optical Coherence Tomography, 2nd ed. (Springer, 2015).
2. E. Beaurepaire, A. C. Boccara, M. Lebec, L. Blanchot, and H. Saint-Jalmes, "Full-field optical coherence microscopy," Opt. Lett. 23(4), 244–246 (1998).
3. B. Grajciar, M. Pircher, A. Fercher, and R. Leitgeb, "Parallel Fourier domain optical coherence tomography for in vivo measurement of the human eye," Opt. Express 13(4), 1131–1137 (2005).
4. B. Grajciar, Y. Lehareinger, A. Fercher, and R. Leitgeb, "High sensitivity phase mapping with parallel Fourier domain optical coherence tomography at 512 000 A-scan/s," Opt. Express 18(21), 21841–21850 (2010).
5. A. F. Zuluaga and R. Richards-Kortum, "Spatially resolved spectral interferometry for determination of subsurface structure," Opt. Lett. 24(8), 519–521 (1999).
6. D. J. Fechtig, B. Grajciar, T. Schmoll, C. Blatter, R. M. Werkmeister, W. Drexler, and R. A. Leitgeb, "Line-field parallel swept source MHz OCT for structural and functional retinal imaging," Biomed. Opt. Express 6(3), 716–735 (2015).
7. L. Ginner, A. Kumar, D. Fechtig, L. M. Wurster, M. Salas, M. Pircher, and R. A. Leitgeb, "Noniterative digital aberration correction for cellular resolution retinal optical coherence tomography in vivo," Optica 4(8), 924 (2017).
8. L. Ginner, T. Schmoll, A. Kumar, M. Salas, N. Pricoupenko, L. M. Wurster, and R. A. Leitgeb, "Holographic line field enface OCT with digital adaptive optics in the retina in vivo," Biomed. Opt. Express 9(2), 472–485 (2018).
9. V. P. Pandiyan, X. Jiang, A. Maloney-Bertelli, J. A. Kuchenbecker, U. Sharma, and R. Sabesan, "High-speed adaptive optics line-scan OCT for cellular-resolution optoretinography," Biomed. Opt. Express 11(9), 5274–5296 (2020).
10. V. P. Pandiyan, X. Jiang, J. A. Kuchenbecker, and R. Sabesan, "Reflective mirror-based line-scan adaptive optics OCT for imaging retinal structure and function," Biomed. Opt. Express 12(9), 5865–5880 (2021).

11. V. P. Pandiyan, A. Maloney-Bertelli, J. A. Kuchenbecker, K. C. Boyle, T. Ling, Z. C. Chen, B. H. Park, A. Roorda, D. Palanker, and R. Sabesan, "The optoretinogram reveals the primary steps of phototransduction in the living human eye," Sci. Adv. 6(37), eabc1124 (2020).

12. L. Han, B. Tan, Z. Hosseinaee, L. K. Chen, D. Hileeto, and K. Bizheva, "Line-scanning SD-OCT for in-vivo, non-contact, volumetric, cellular resolution imaging of the human cornea and limbus," Biomed. Opt. Express 13(7), 4007–4020 (2022).

13. A. Davis, O. Levecq, H. Azimani, D. Siret, and A. Dubois, "Simultaneous dual-band line-field confocal optical coherence tomography: application to skin imaging," Biomed. Opt. Express 10(2), 694–706 (2019).

14. A. Dubois, O. Levecq, H. Azimani, A. Davis, J. Ogien, D. Siret, and A. Barut, "Line-field confocal time-domain optical coherence tomography with dynamic focusing," Opt. Express 26(26), 33534–33542 (2018).

15. A. Dubois, W. Xue, O. Levecq, P. Bulkin, A.-L. Coutrot, and J. Ogien, "Mirau-based line-field confocal optical coherence tomography," Opt. Express 28(6), 7918–7927 (2020).

16. E. Cinotti, M. Bertello, A. Cartocci, D. Fiorani, L. Tognetti, V. Solmi, S. Cappilli, K. Peris, J. L. Perrot, M. Suppa, V. Del Marmol, and P. Rubegni, "Comparison of reflectance confocal microscopy and line-field optical coherence tomography for the identification of keratinocyte skin tumours," Ski. Res. Technol. 29(1), e13215 (2023).

17. I. Powell, "Design of a laser beam line expander," Appl. Opt. 26(17), 3705–3709 (1987).

18. Z. Al-Qazwini, Z. Y. G. Ko, K. Mehta, and N. Chen, "Ultrahigh-speed line-scan SD-OCT for four-dimensional in vivo imaging of small animal models," Biomed. Opt. Express 9(3), 1216–1228 (2018).

19. ANSI Z80.36-2016, Ophthalmics, Light Hazard Protection for Ophthalmic Instruments.

20. S. Saghafi, K. Becker, C. Hahn, and H.-U. Dodt, "3D-ultramicroscopy utilizing aspheric optics," J. Biophotonics 7(1-2), 117–125 (2014).

21. B. Cense, N. A. Nassif, T. C. Chen, M. C. Pierce, S.-H. Yun, B. H. Park, B. E. Bouma, G. J. Tearney, and J. F. de Boer, "Ultrahigh-resolution high-speed retinal imaging using spectral-domain optical coherence tomography," Opt. Express 12(11), 2435–2447 (2004).

22. J. Lu, B. Gu, X. Wang, and Y. Zhang, “High speed adaptive optics ophthalmoscopy with an anamorphic point spread function,” Opt. Express 26(11), 14356–14374 (2018).

23. S. Chen, X. Liu, N. Wang, X. Wang, Q. Xiong, E. Bo, X. Yu, S. Chen, and L. Liu, “Visualizing micro-anatomical structures of the posterior cornea with micro-optical coherence tomography,” Sci. Rep. 7(1), 10752 (2017).

24. Y.-T. Chen, C.-Y. Tsai, Y.-K. Chiu, T.-W. Hsu, L. W. Chen, W.-L. Chen, and S.-L. Huang, “En face and cross-sectional corneal tomograms using sub-micron spatial resolution optical coherence tomography,” Sci. Rep. 8(1), 14349 (2018).

25. M. Ang, A. Konstantopoulos, and G. Goh, et al., “Evaluation of a micro-optical coherence tomography for the corneal endothelium in an animal model,” Sci. Rep. 6(1), 29769 (2016).

26. S. G. Adie, B. W. Graf, A. Ahmad, P. S. Carney, and S. A. Boppart, “Computational adaptive optics for broadband optical interferometric tomography of biological tissue,” Proc. Natl. Acad. Sci. U. S. A. 109(19), 7175–7180 (2012).

27. A. Kumar, W. Drexler, and R. A. Leitgeb, “Numerical focusing methods for Full Field OCT: a comparison based on a common signal model,” Opt. Express 22(13), 16061–16078 (2014).

28. D. Borycki, E. Auksorius, P. We ̨grzyn, and M. Wojtkowski, “Computational aberration correction in spatiotemporal optical coherence (STOC) imaging,” Opt. Lett. 45(6), 1293–1296 (2020).

29. A. Kumar, T. Kamali, R. Platzer, A. Unterhuber, W. Drexler, and R. A. Leitgeb, “Anisotropic aberration correction using region of interest based digital adaptive optics in Fourier Domain OCT,” Biomed. Opt. Express 6(4), 1124–1134 (2015).

30. M. F. Kraus, B. Potsaid, M. A. Mayer, R. Bock, B. Baumann, J. J. Liu, J. Hornegger, and J. G. Fujimoto, “Motion correction in optical coherence tomography volumes on a per a-scan basis using orthogonal scan patterns,” Biomed. Opt. Express 3(6), 1182–1199 (2012).

Chapter 4
Powell lens-based Line-Field OCT for in-vivo, contact-less, cellular resolution imaging of the human cornea

4.1 Introductions

The cornea is the transparent multilayered tissue at the front part of the eye that accounts for approximately two-thirds of the eye's total refractive power [1]. Degenerative, infectious and inherited corneal pathologies such as keratoconus, Fuch's dystrophy, etc. constitute the 4th leading cause of blindness worldwide after cataract, glaucoma, and age-related macular degeneration [2], At the early stages of their development, these diseases alter the corneal morphology at the cellular level. Therefore, the early diagnostic of corneal pathologies and the effective planning of therapeutic approaches are strongly dependent on the ability of imaging technologies to visualize, identify, and characterize the cellular structure of the cornea in-vivo.

Over the past three decades, different designs of OCT technology were utilized for imaging the human cornea in-vivo. Point-scanning spectral-domain (SD) OCT offers the advantage of ultrahigh resolution, in the order of 1 μm in the corneal tissue, by utilizing broadband light sources [3-9]. However, the relatively slow image acquisition rates in those studies (< 100 kHz) prevented acquisition of volumetric OCT images due to presence of strong, involuntary eye motion artefacts. Our research group utilized a linear-array camera with 250 kHz image data acquisition rate to generate in a contactless way the first, in-vivo, volumetric SD-OCT images of the healthy human cornea with spatial resolution sufficient to visualize the cellular structure of all corneal layers [10]. However, eye motion artifacts were still noticeable in the 3D images and the Field-of-View (FOV) was restricted to less than $200 \times 200\ \mu m^2$.

Full-field (FF) time-domain (TD) OCT combines very high transverse resolution (~1 μm) and relative insensitivity of the images to optical aberrations [11-13], which allows FF-TD-OCT to image the cellular structure of the human corneal stroma and endothelium both ex-vivo [14-16] and in-vivo [17, 18]. However, FF-TD-OCT was not able to resolve cells in the corneal epithelium due to the limited dynamic range of the area camera, resulting in limited Signal-to-Nosie Ratio (SNR) [18]. FF swept-source (SS) OCT utilizes a rapidly tunable light source to generate high resolution, volumetric images of the human cornea. This technology offers better sensitivity and faster volumetric acquisition rate

compared to FF-TD-OCT, as well as high phase stability of the enface OCT images, necessary for digital correction of aberrations [19]. However, the axial resolution of FF-SS-OCT technology is limited to ~5 μm in corneal tissue due to the fairly narrow tunable range of the light source, which is insufficient for visualization and precise morphometry of the thin corneal layers such as the endothelium and the pre-Descemet's layer, whose thickness is comparable to the FF-SS-OCT axial resolution.

Line-Field SD-OCT (LF-SD-OCT) offers a much faster data acquisition rate compared to point-scanning SD-OCT, by projecting a line-shaped beam onto the imaged object, scanning the beam only in one direction and utilizing an ultrafast area camera at the detection end of the system. Although the concept of LF-OCT was published more than two decades ago [20], the use of this technology for in-vivo imaging of the human retinal structure and blood flow [21] and the retinal response to visual stimulation [22] was only reported recently. Our research group pioneered the use of LF-SD-OCT for in-vivo human corneal imaging and demonstrated that the combination of high spatial resolution and fast imaging allows for volumetric visualization of the corneal cellular structure [23]. A more recent publication from another research group reported a cylindrical lens-based LF-SD-OCT system with more affordable light source and area camera [24]. However, the significantly lower system sensitivity and axial resolution resulted in overall reduced quality of the human corneal images. One limitation of the original design of our corneal LF-SD-OCT system was the use of a cylindrical lens as the line generator. This resulted in a Gaussian distribution of the optical power along the length and width of the line-shaped beam, which contributed to > 10 dB sensitivity loss between the center and the edges of the LF-SD-OCT corneal images. Recently, our research group explored the use of a Powell lens as the line generator in a LF-SDOCT system that offers a "Top-Hat" optical power distribution along the length of the line beam [25]. The use of the Powell lens reduced the sensitivity roll off from the center to the edges of the LF-SD-OCT images to < 3 dB and allowed for significant expansion of the FOV. However, technical limitations with the area camera, the optical design and the light source prevented the use the first-generation Powell lens-based LF-SD-OCT (PL-LF-SD-OCT) system for in-vivo human corneal imaging.

In this paper, we present a novel and significantly improved design of the PL-LF-SD-OCT system. The new design offers ~ 2.4 μm × 2.2 μm × 1.7 μm (x × y × z) resolution in biological tissue assuming an average refractive index of 1.38, maximum sensitivity of ~ 90 dB measured for data acquisition rate of 2,400 frames per second (fps) and 2.6 mW optical power incident on the corneal surface.

4.2 Methods

4.2.1 System's design

The first-generation PL-LF-SD-OCT system published recently by our research group [25] had some limitations in terms of sensitivity, sensitivity roll-off, balance between transverse resolution and depth of focus (DOF) and camera triggering issues that limit the scanning direction FOV and prevent the safe, in-vivo, contactless imaging of the human cornea. In the second-generation PL-LF-SD-OCT system design presented here, the light source and camera were replaced with alternate options to improve the system's sensitivity and resolve the camera triggering issues. The system's optical design was also revised for better control of the sensitivity roll-off, finer digital resolution both in illumination line direction and spectral direction, and optimal trade-off between transverse resolution and DOF and expand DOF by ~2.5 times, which is important for in-vivo cellular resolution corneal imaging where involuntary eye motion in the axial direction can cause significant defocus and distortions of the OCT images. Detailed description of the new system design is presented below.

At the first step, the optical design of the new PL-LF-SD-OCT system was simulated in Zemax OpticStudio (Ansys Inc.), assuming a central wavelength of 850 nm. AutoCAD and Inventor (Autodesk Inc.) were used to generate 2D and 3D mechanical layouts of the system based on the Zemax simulation, and a 3D printer (Photon M3 Premium, ANYCUBIC) was used to print some of the optomechanical components. The system was assembled on a 30 × 30 $inch^2$ optical breadboard, with lens positions constrained precisely by 3D-printed spacers. A schematic diagram of the novel PL-LF-SD-OCT system is presented in Fig. 4.1, where the major components that were replaced relative to the original design are marked with red dashed lines.

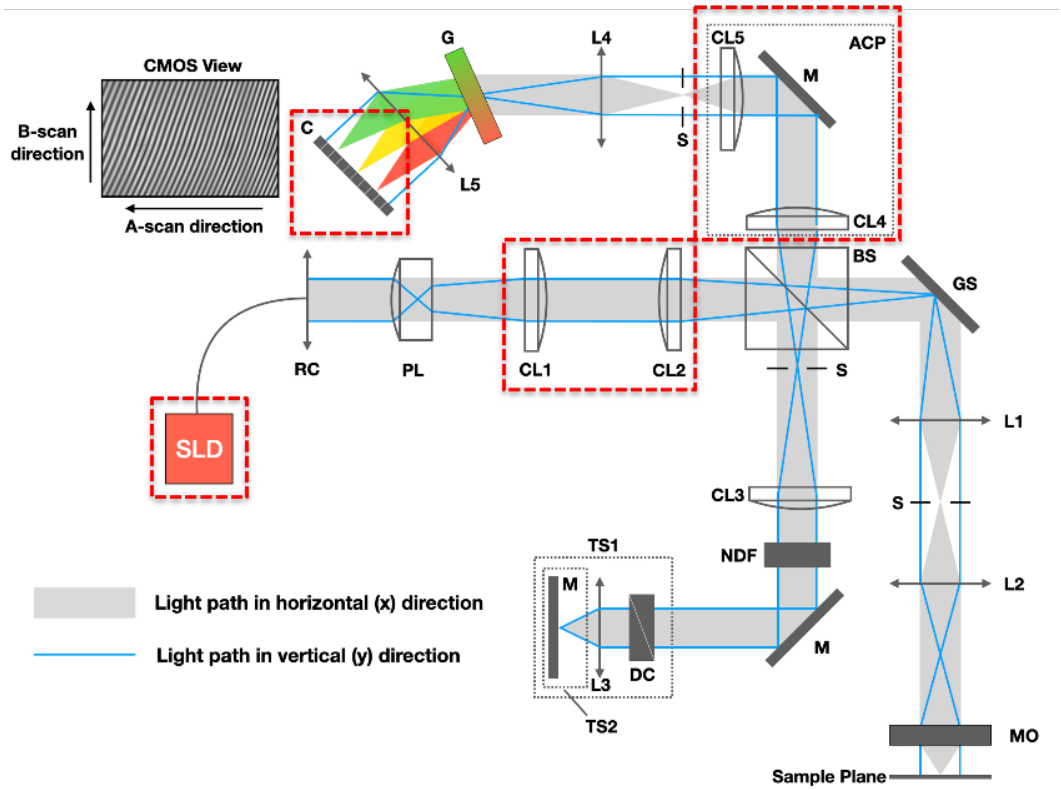

Fig. 4.1. PL-LF-SD-OCT system layout. SLD: Superluminescent Diodes; RC: reflective collimator; PL: Powell lens; CL: cylindrical lens; BS: beamsplitter; GS: galvanometric scanner; L1-L3 and L5: achromatic doublet lens; G: grating; L6: camera lens; C: camera; S: slit; NDF: neutral density filter; M: mirror; TS: translation stage; DC: dispersion compensation unit. PL = 5º fan angle, CL1 = CL5 = 75 mm, CL2 = CL3 = 100 mm, L1 = 80 mm, L2 = 100 mm, L3 = 40 mm, L5 = 125 mm, L6 = 85 mm.

4.2.1.1 Light source

The original PL-LF-SD-OCT system design [25] utilized a supercontinuum light source (SuperK, NKT Photonics, Denmark), which has elevated relative intensity noise (RIN) that resulted in an overall reduced system's sensitivity. In the new design presented here, a custom broadband light source (cBLMD-T-850-HP, Superlum) comprised of three superluminescent diodes (SLDs) whose emissions that can be controlled individually, was utilized. The default version of this light source has an almost "Top-Hat" emission spectrum with some intensity modulations. For our study, the light source was customized to increase the spectral power of the emission spectrum at longer wavelengths in order to

compensate for the significant wavelength-dependent decrease of the camera's quantum efficiency (QE). Fig. 4.2A shows the emission spectrum of the customized broadband light source as measured with a spectrum analyzer, as well as the QE response curve of the new camera (PCO, Germany).

Figure 4.2B shows the sample and reference arms spectra of the interferometer, measured using silver-protected mirrors as targets. The two spectra have almost identical 3dB bandwidths of ~170 nm, centered at ~840 nm, resulting in axial point-spread function (PSF) of ~2.3 μm in free space, corresponding to ~1.7 μm in biological tissue assuming an average refractive index of 1.38 (Fig. 4.2C). The axial PSF displayed in Fig. 4.2C was generated by zero-padding the raw data before applying a Fast Fourier Transform (FFT). Both hardware (HDC) and software dispersion compensation (SDC) were applied to generate a symmetric axial PSF.

4.2.1.2 Illumination and detection arm

The illumination arm of the PL-LF-SD-OCT system is similar to the previously published version [24] with one major modification: the achromat doublets lens pair following the Powell lens was replaced with a cylindrical lens pair of the same focal lengths. This modification removed the magnification power applied in the X direction of the light by the original achromat doublets pair. This modification resulted in ~ 2.5 times extension of the system's DOF with minimal change to the transverse resolution in the X direction. The extension of the DOF while preserving the system's transverse resolution facilitated the in-vivo acquisition of volumetric images of the human cornea.

In LF-OCT technology, the lens that generates the line-beam also decouples light propagation in the X and Y directions. The digital OCT resolution in the scanning direction, referred to as the X direction in this study, mirrors that of point-scanning SD-OCT systems and is dependent on the magnification power of the optical design, the pixel size of the area camera and the density of the scanning. However, the digital resolution in the line direction, or the Y direction in this study, is dependent on the total magnification power of the system in the line direction of the detection arm, as well as the camera pixel size. To adhere to the Nyquist-Shannon Sampling Theorem for signal processing, a high line-direction magnification power is needed to achieve cellular resolution. This, however, results in reduced magnification power in the X direction, or equivalently, a smaller incident light spot diameter before the camera due to the inverse conjugation between the XY magnification powers. This results in a larger focusing spot projected onto the camera sensor, introducing crosstalk between consecutive A- and B-scans. In the new design of the PL-LF-SD-OCT system, we implemented an anamorphic cylindrical

lens pair design to control the system's magnification in the X and Y directions independently [26, 27]. This modification allows for a much more flexible optical design of the entire system.

The spectrometer at the detection end of the PL-LF-SD-OCT system was redesigned to include a new ultrahigh-speed area camera (pco.dimax cs4, PCO), featuring a full pixel range of 2016×2016 and a pixel size of 11×11 μm^2. The larger pixel size contributed to the overall higher SNR of the new PL-LF-SD-OCT system. Note that the new system design utilized only 1680 pixels in the spectral direction since the SLD light source has somewhat smaller spectral bandwidth compared to the SuperK supercontinuum laser used in the original design of the system [24], and 600 pixels in the line direction. The camera acquisition speed (B-scan rate) was set at ~2,380 fps, which is equivalent to an A-scan rate of ~1.43 MHz. With the current selection of the active pixel region (1680 × 600), the maximum achievable frame rate is ~4,400 fps (equivalent to 2.64 MHz A-scan rate), though increasing the camera rate to maximum while keeping all other factors the same would result in ~ 2.5 dB sensitivity drop.

4.2.1.3 System performance

Figure 4.2 summarizes the performance test results for the new PL-LF-SD-OCT system, that were conducted with ~2.6 mW optical imaging power incident on the imaged target and with image acquisition rate of 2,380 fps. Fig. 4.2D shows the sensitivity roll-off of the PL-LF-OCT system. The maximum sensitivity of 90.4 dB was measured at a depth of 100 μm, with 18dB sensitivity roll off over a scanning range of 1,400 μm. Fig. 4.2E shows the axial PSF width as a function of scanning depth. The axial PSF width remains at approximately 2.2 μm in free space for the initial 1.1 mm depth, then diverges to roughly 2.6 μm up to a scanning depth of 1.4 mm. This trend correlates with an almost 10 dB sensitivity drop for depth locations between 1.1 mm and 1.4 mm. The most likely cause for this trend is the divergence of the optical beam in the reference arm of the system caused by the Powell lens.

Figure 4.2F shows the B-scan sensitivity as a function of pixel, measured across all 600 pixels at an imaging depth of 100 μm. The novel design of the PL-LF-SD-OCT system results in only ~2.6 dB sensitivity difference between the center and the edges of the B-scan. Figure 4.2G shows a zoomed-in image of Group 6 and Element 7 of a reflective USAF 1951 resolution target acquired with the new PL-LF-Sd-OCT system. The coherence edge spread functions (cESFs) from the line direction and the scanning direction shown in Figures 4.2H and 4.2I respectively, generated from the data shown in Fig. 4.2G, can be used to determine the system's lateral resolution. This resolution is defined as twice the

Full-Width-at-Half-Maximum (FWHM) of the coherence line spread function (cLSF) and can be calculated by taking the derivative of the cESFs. Using this methodology, the system's lateral resolution is measured to be 2.4 µm in the X direction and 2.18 µm in the Y direction.

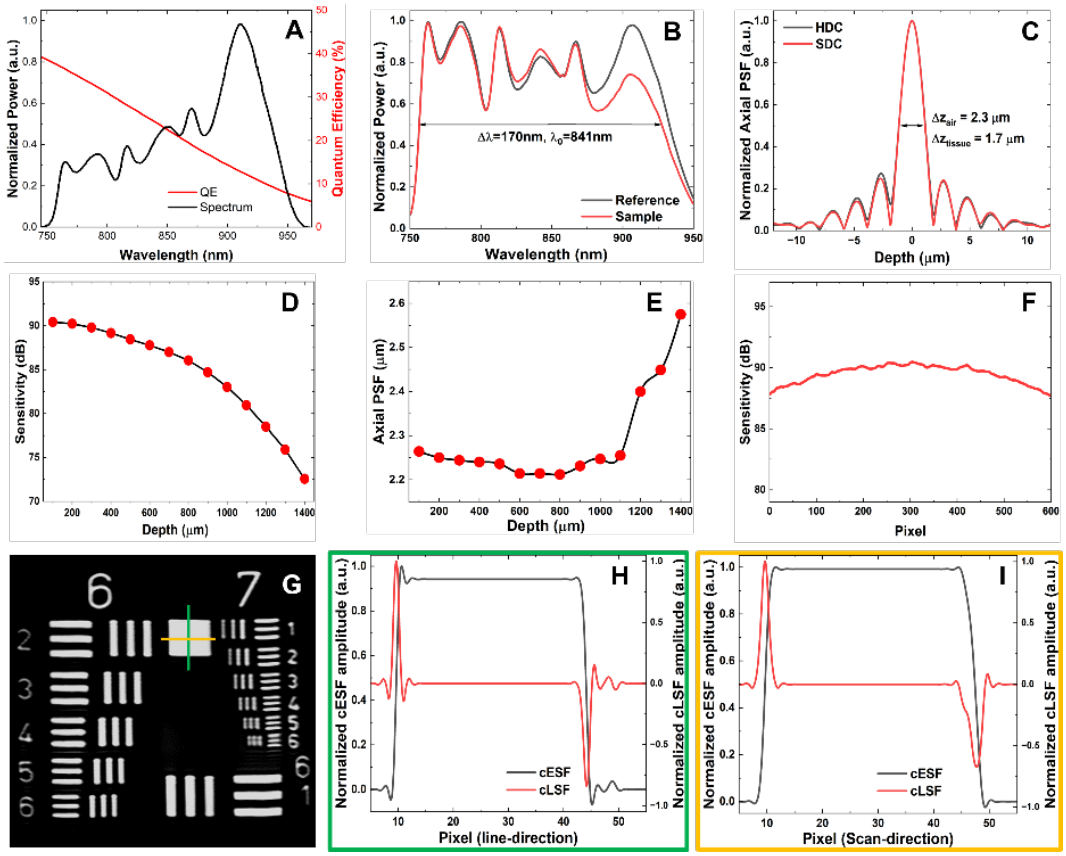

Fig. 4.2. (A) Emission spectrum of the customized SLD and QE of the camera. (B) Reference and sample arms spectra measured at the detection end of the PL-LF-SD-OCT system. (C) System's axial PSF measured in free space at a scanning depth of ~100 µm. Black line shows PSF after hardware dispersion compensation (HDS) only, while the red line shows the PSF after software dispersion compensation. (D) Sensitivity roll-off. (E) Axial PSF width as a function of scanning depth. (F) B-scan sensitivity across pixels in the scan direction. (G) Image of an USAF target. (H and I) lateral PSFs for the line and scan directions.

4.2.2 Imaging protocol and imaging processing

In-vivo human cornea imaging with the PL-LF-SD-OCT system has received full ethics clearance from the Research Ethics Office at the University of Waterloo. Corneal images were acquired from a 26-

year-old healthy male volunteer. The subject's head was gently secured in a custom head support frame attached to XYZ translation stages to allow for alignment of the imaged eye with respect to the optical imaging beam. The imaging optical power incident on the corneal surface was 2.6 mW, which is significantly lower than the maximum permissible exposure for the human cornea and retina imaging, as stipulated by the ANSI standard [28]. Volumetric datasets comprising of 1,680 A-scans and 600 B-scans were acquired at a rate of 2,380 fps. The corresponding FOV was 570 μm × 620 μm (X × Y). The acquisition duty cycle for one dataset is completed within 0.3 seconds, including the response times from the scanner and the camera.

The raw PL-LF-SD-OCT images were dispersion compensated numerically, followed by cross-correlation of consecutive B-scans to compensate for any involuntary eye motion. Afterwards, the images were flattened to compensate for the natural curvature of the cornea and allow for generation of flat enface images from different depths inside the cornea. For the flattening procedure, the corneal curvature was mapped separately for the XZ and YZ B-scans using a maximum intensity projection (MIP) method, by using the anterior surface of the corneal epithelium or the posterior surface of the corneal endothelium. A mask filter was applied to the MIP data to eliminate erroneously counted data from other regions, followed by a high-order polynomial fit applied to the reference curve. The volumetric dataset was flattened separately based on the XZ and YZ fits.

A novel algorithm was developed for sharpening and suppressing speckle noise in the volumetric PL-LF-SD-OCT images. Briefly, the algorithm is based on the following principle: First, speckle in log-scale images is modeled as a stationary correlated noise. Subsequently, the derived model is fed into a self-similarity-based model alongside a log-scale intensity image to derive non-local structural priors. Moreover, the priors are integrated into a maximum-a-posteriori (MAP) reconstruction framework with additional regularization terms such as total variation (TV). The MAP framework generates a speckle-free and aberration-reduced image.

4.3 Results

Considering that the DOF of the current design of the PL-LF-SD-OCT system was ~30 μm, while the typical total human cornea thickness is in the range of 500 to 600 μm, volumetric images of the anterior, middle and posterior regions of the cornea were acquired separately by translating the image focal at the desired depth within the cornea.

4.3.1 Anterior cornea

Figure 4.3 summarizes PL-LF-SD-OCT images acquired from the anterior cornea. Fig. 4.3A shows a volumetric image of the corneal epithelium and anterior stroma. The green arrow marks highly reflective features in the tear film layer that most like correspond to cellular debris. A representative B-scan from the volumetric data set is presented in Fig. 4.3B. The cellular structure of the corneal epithelium (EPI) and he boundaries of the Bowman's membrane (BM) are clearly visible. Keratocytes in the stroma (STR) appear white reflective dashes. Since the focal plane was located close to the EPI/BM boundary and the DOF was about 2 time smaller than the thickness of the corneal EPI, both the superficial EPI cells and keratocytes located farther away from the BM surface appear blurred. The small reflective feature at the EPI/BM boundary, marked with the red arrow corresponds to a cross-section of a sub-basal cornea nerve. An enface image of the EPI/BM interface generated from the volumetric data set shows a group of sub-basal corneal nerves (Fig. 4.3C). The dark horizontal lines in the image correspond to fast axial eye motion that causes defocus in the OCT images and resulted in lower image contrast.

Figures 4.3D-4.3F show enface images of the wing cells of the corneal EPI for different magnifications. Individual epithelial cells are resolved over a FOV of ~ 550 μm × 550 μm (Fig. 4.3D), while individual cellular nuclei are resolved under higher magnification from the same data set (Fig. 4.3F, red arrows).

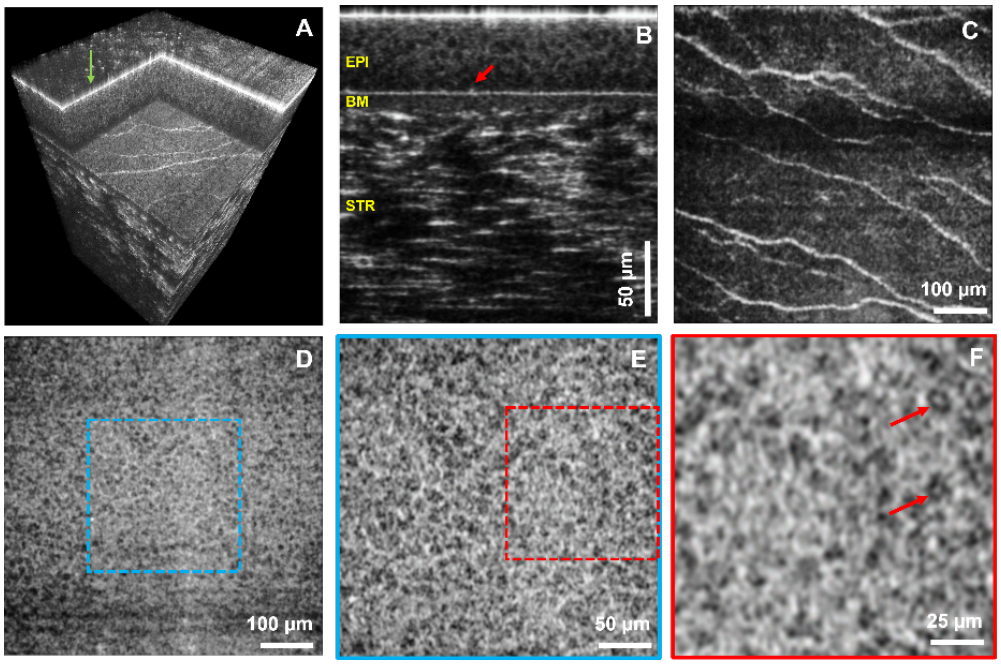

Fig. 4.3. PL-LF-SD-OCT images of the anterior human cornea. (A) Volumetric image. Green arrow marks hyper-reflective structures in the tear film. (B) B-scan showing the cellular structure. EPI: epithelium, BM: Bowman's membrane, STR: Stroma. (C) Enface image of sub-basal nerves. (D-F) Enface images of the wing cells in the corneal EPI under different magnification. Red arrows in (F) mark reflections from cellular nuclei.

4.3.2 Corneal stroma

Figure 4.4 shows PL-LF-SD-OCT images acquired at different depth locations in the corneal stroma. Figures 4.4A-4.4D show the original images, while Figures 4.4E-4.4H show the same images after processing with the novel image processing algorithm. High density, smaller sized keratocytes are observed close to the BM/ STR interface (Figs. 4.4A and 4.4E). The density of the keratocytes decreases progressively with depth, while their size increases (Figs 4.4B, 4.4C, 4.4F and 4.4G). A thin stromal nerve is visible in the anterior stroma (Figs 4.4C and 4.4G). The density of keratocytes in the posterior stroma, close to the Descemet's membrane (DM) is very low and thin processes connecting the individual cells are observed in the images (Figs. 4.4D and 4.4H).

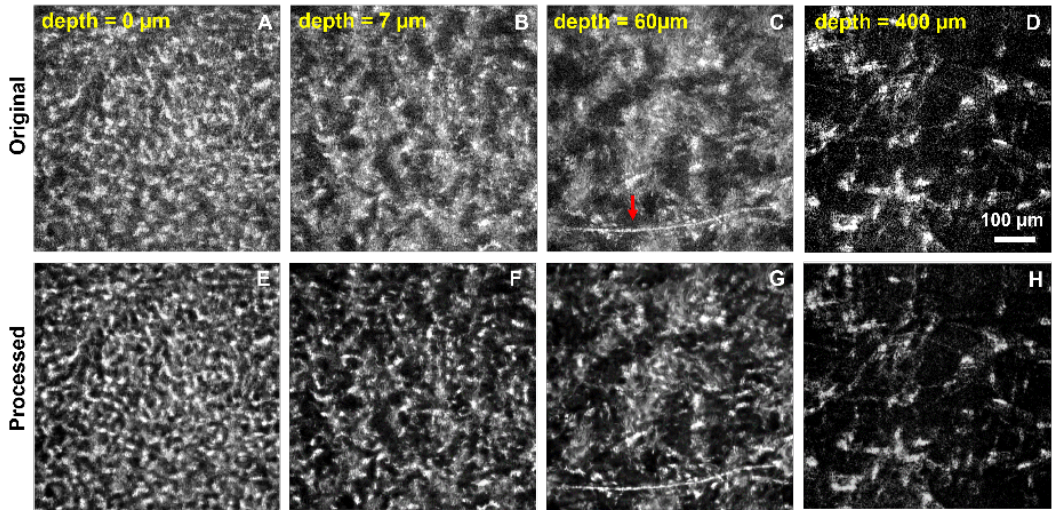

Fig. 4.4. PL-LF-SD-OCT images of the corneal stroma acquired at different depth locations relative to the BM/STR interface. (A-D) raw images. (E-H) same images processed with the novel image processing algorithm.

4.3.3 Posterior cornea

Figure 4.5 shows PL-LF-SD-OCT images acquired from the posterior cornea. A volumetric image is shown in Fig. 4.5A. Residual eye motion artefacts are visible in the scan direction. A representative B-scan is shown in Fig. 4.5B, where the imaging plane was focused close to the posterior surface of the endothelial layer (END). The image clearly shows the multi-layered structure of the posterior cornea. Fig. 4.5C shown the same image with boundaries of the END, the Descemet's membrane (DM) and the pre-Descemet's layer (PDL) are marked with red and blue dashed lines respectively. The system's digital axal resolution is high enough not only to visualize these 3 corneal layers, but also to measure their average thickness: END – 5.2 µm, DM – 7.4 µm and PDL – 4.7 µm. These values agree well with data from anatomical studies [6, 29]. Fig. 4.5D shows a B-scan from the scanning direction, generated from the volumetric data set. While the 3 posterior corneal layers are clearly identified in the image, residual eye motion artefact was present that caused challenges in generating enface images of the END that were in-focus over the entire FOV. Enface images of the corneal END that were generated using MIP over the thickness of the END layer, are shown in Figs. 4.5E and 4.5F under different magnification. While the cellular structure of the END is clearly visible in both images, the eye-motion induced blur is visible in some locations of the image in Fig. 4.5E.

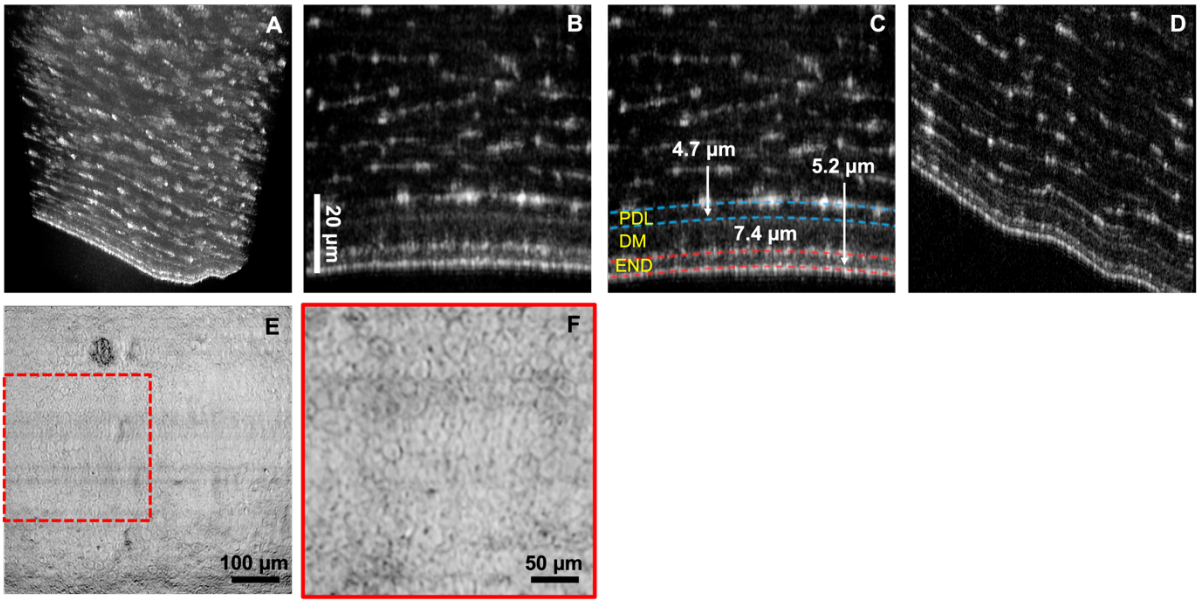

Fig. 4.5. PL-LF-SD-OCT images of the posterior human cornea. (A)Volumetric image. (B) B-scan of posterior human cornea. (C) B-scan of posterior human cornea with different layers labelled. (D) YZ (scanning direction) view of the posterior human cornea. (E) Enface view of endothelium cells. (F) magnetified region from (E).

4.4 Discussion

1) **Light source and spectral shape**: the SLD used in this study offered a low RIN, which allowed for ~1.5 dB improvement of the sensitivity of the new PL-LF-SD-OCT system for the same optical imaging power, compared to the supercontinuum light source reported in our previous study [25]. The uneven emission power of the SLD channels resulted in an almost top-hat detection spectrum on the spectrometer side, yielding a measured axial resolution close to the theoretical value that this light source could achieve (~2.26 µm measured vs. ~2.06 µm theoretical). The infrared (IR) side of the sample arm spectrum (Fig. 4.2B) appears to have lower intensity than expected. Given that the two arms share most of the optical path, use lenses from the same manufacturer with the same coating within each arm, and the spectrum is measured with the same reflective mirror, it is likely that this difference is associated with the transmission function of the microscopic objective or chromatic aberrations.

2) **Sensitivity**: The novel PL-LF-SD-OCT system achieved sensitivity of ~90 dB at a 100 µm depth for acquisition speed of ~2,400 fps and incident power of about 2.6 mW. For comparison, our previously reported system [25] achieved maximum sensitivity of ~ 87 dB at a 100 µm depth with an acquisition

speed of ~2,000 fps and an incident power of ~2.5 mW. The enhanced SNR is primarily due to three factors: a) the lower RIN of the SLD light source, b) the larger pixel size and increased quantum well capacity of the PCO camera, and c) the higher QE of the PCO camera at the same wavelength. The improved sensitivity enables the new PL-LF-SD-OCT system to resolve low-contrast structures, such as the epithelial wing cells, a feat that was not achievable with the previous system, despite its higher spatial resolution.

3) **Correction of eye motion artefacts**: The flattening algorithm discussed in section 4.3 can enhance enface visualization by compensating for the inherent curvature of the cornea as well as eye movements. However, it does not aid in correcting defocusing caused by motion, nor the shift in focus due to the curvature of the eye. As illustrated in Figs. 4.3C, 4.3D, 4.5D and 4.5F, even at image acquisition rates of ~2,400 fps, it is still likely to capture fast axial motion in the range of 50 – 70 μm, which causes defocusing of the corneal images and reduces the visibility of epithelial and endothelial cells. To address this issue, three improvements could be considered: a) Further reducing the lateral resolution to increase the DOF. Currently, the system has a DOF of ~30 μm for a scanning lateral resolution of ~2.4 μm. Lowering it to ~3 μm could provide an additional 20-μm DOF. However, this could result in the inability to resolve cellular structures when in focus, and also spread the incident energy over a larger axial range, lowering the contrast of the image within the coherence length plane. b) Further increasing the acquisition speed for an even shorter volumetric data acquisition period. Doubling the acquisition speed could reduce eye motion from ~50-70 μm to ~25-35 μm, assuming a linear trend. However, this approach will result in ~3 dB sensitivity loss in sensitivity and affect the system's ability to resolve low contrast structures such as epithelial cells. c) Using Adaptive Optics (AO) or Digital Adaptive Optics (DAO) to correct defocus aberration. While the hardware approach could lead to a more complex and expensive system design and pose challenges to system alignment and maintenance, the DAO approach, especially correction for chromatic source defocusing is feasible and is currently under investigation.

4) **Powell lens and light spectrum uniformity**: In our previous study, we reported a line direction sensitivity fluctuation of ~1.6 dB, and for the current study, a ~2.6 dB fluctuation. The decrease in sensitivity uniformity stems from two primary factors: a) The Powell lens used in this study is designed based on visible wavelength monochromatic light. The emission spectrum we are working with for this study has a similar full spectral bandwidth compared to the previous study but is more shifted towards the IR region. This shift towards the IR spectrum has degraded the lens performance. It is possible to

design the Powell lens achromatically with a secondary surface added for chromatic aberration correction, similar to achromatic doublet lenses. However, to our best knowledge, no such product has been released yet. b) The line direction digital resolution is determined by the ratio of pixel size to line direction magnification power. The camera pixel size in this study is larger than before (11 μm compared to 7.8 μm), while we designed a digital resolution even higher than before (1.05 μm compared to 1.1 μm). This approach magnifies the line to a larger size, causing the edge of the line to pass through more off-axis lens regions than before, thereby experiencing degraded lens performance. This issue could be resolved by working with smaller camera pixels, reducing the desired digital resolution, or working with a larger diameter lens. It is crucial to note that due to the overall increase in the system's SNR performance, even the point with the lowest SNR on the line in this study still has a higher SNR than the maximum SNR measured in the previous study.

4.5 Conclusion

We have developed a new design for a PL-LF-SD-OCT system with improved sensitivity, larger FOV and demonstrate the suitability of the system for in-vivo, contactless, volumetric imaging of the human cornea. Healthy corneal images acquired with this system showed that the combination of high spatial resolution, fast image acquisition rate and improves sensitivity are sufficient to visualize individual cells and cellular nuclei in the high contrast PL-LF-SD-OCT images, as well as carry out morphometric analysis on the thin corneal layers (END, DM, PDL and BM). Future applications of this novel technology will include clinical studies of various corneal pathologies.

4.6 References

1. D. M. Maurice, "The structure and transparency of the cornea". The Journal of Physiology. 136 (2): 263–286.1. (1957).
2. M. S. Oliva, T. Schottman, and M. Gulati, "Turning the tide of corneal blindness," Indian J Ophthalmol 60(5), 423–427 (2012).
3. R. Yadav, K.-S. Lee, J. P. Rolland, J. M. Zavislan, J. V. Aquavella, and G. Yoon, "Micrometer axial resolution OCT for corneal imaging," Biomedical Optics Express 2(11), 3037–3046 (2011).
4. R. M. Werkmeister, A. Alex, S. Kaya, A. Unterhuber, B. Hofer, J. Riedl, M. Bronhagl, M. Vietauer, D. Schmidl, T. Schmoll, G. Garhöfer, W. Drexler, R. A. Leitgeb, M. Groeschl, and L. Schmetterer, "Measurement of Tear Film Thickness Using Ultrahigh-Resolution Optical Coherence Tomography," Investigative Opthalmology Vis Sci 54(8), 5578 (2013).

5. P. Tankam, Z. He, Y.-J. Chu, J. Won, C. Canavesi, T. Lepine, H. B. Hindman, D. J. Topham, P. Gain, G. Thuret, and J. P. Rolland, "Assessing microstructures of the cornea with Gabor-domain optical coherence microscopy: pathway for corneal physiology and diseases," Opt Lett 40(6), 1113 (2015).
6. K. Bizheva, L. Haines, E. Mason, B. MacLellan, B. Tan, D. Hileeto, and L. Sorbara, "In Vivo Imaging and Morphometry of the Human Pre-Descemet's Layer and Endothelium With Ultrahigh-Resolution Optical Coherence Tomography.," Invest Ophth Vis Sci 57(6), 2782–7 (2016).
7. K. Bizheva, B. Tan, B. MacLelan, O. Kralj, M. Hajialamdari, D. Hileeto, and L. Sorbara, "Sub-micrometer axial resolution OCT for in-vivo imaging of the cellular structure of healthy and keratoconic human corneas.," Biomedical optics express 8(2), 800–812 (2017).
8. S. Chen, X. Liu, N. Wang, X. Wang, Q. Xiong, E. Bo, X. Yu, S. Chen, and L. Liu, "Visualizing Micro-anatomical Structures of the Posterior Cornea with Micro-optical Coherence Tomography," Sci Rep-uk 7(1), 10752 (2017).
9. X. Yao, K. Devarajan, R. M. Werkmeister, V. A. dos Santos, M. Ang, A. Kuo, D. W. K. Wong, J. Chua, B. Tan, V. A. Barathi, and L. Schmetterer, "In vivo corneal endothelium imaging using ultrahigh resolution OCT," Biomed Opt Express 10(11), 5675 (2019).
10. B. Tan, Z. Hosseinaee, L. Han, O. Kralj, L. Sorbara, and K. Bizheva, "250 kHz, 1.5 μm resolution SD-OCT for in-vivo cellular imaging of the human cornea.," Biomedical optics express 9(12), 6569–6583 (2018).
11. A. Dubois, L. Vabre, A.-C. Boccara, and E. Beaurepaire, "High-resolution full-field optical coherence tomography with a Linnik microscope.," Appl Optics 41(4), 805–12 (2002).
12. A. Dubois, K. Grieve, G. Moneron, R. Lecaque, L. Vabre, and C. Boccara, "Ultrahigh-resolution full-field optical coherence tomography," Appl Optics 43(14), 2874 (2004).
13. R. A. Leitgeb, "En face optical coherence tomography: a technology review [Invited].," Biomed Opt Express 10(5), 2177–2201 (2019).
14. K. Grieve, M. Paques, A. Dubois, J. Sahel, C. Boccara, and J.-F. L. Gargasson, "Ocular tissue imaging using ultrahigh-resolution, full-field optical coherence tomography.," Invest Ophth Vis Sci 45(11), 4126–31 (2004).
15. M. Akiba, N. Maeda, K. Yumikake, T. Soma, K. Nishida, Y. Tano, and K. P. Chan, "Ultrahigh-resolution imaging of human donor cornea using full-field optical coherence tomography," J Biomed Opt 12(4), 041202-041202–7 (2007).

16. W. Ghouali, K. Grieve, S. Bellefqih, O. Sandali, F. Harms, L. Laroche, M. Paques, and V. Borderie, "Full-Field Optical Coherence Tomography of Human Donor and Pathological Corneas," Curr Eye Res 40(5), 526–534 (2015).
17. V. Mazlin, P. Xiao, E. Dalimier, K. Grieve, K. Irsch, J.-A. A. Sahel, M. Fink, and A. C. Boccara, "In vivo high resolution human corneal imaging using full-field optical coherence tomography.," Biomedical optics express 9(2), 557–568 (2018).
18. V. Mazlin, P. Xiao, J. Scholler, K. Irsch, K. Grieve, M. Fink, and C. A. Boccara, "Real-time non-contact cellular imaging and angiography of human cornea and limbus with common-path full-field/SD OCT," Nat Commun 11(1), 1868 (2020).
19. E. Auksorius, D. Borycki, P. Stremplewski, K. Liżewski, S. Tomczewski, P. Niedźwiedziuk, B. L. Sikorski, and M. Wojtkowski, "In vivo imaging of the human cornea with high-speed and high-resolution Fourier-domain full-field optical coherence tomography," Biomed Opt Express 11(5), 2849 (2020).
20. A. Zuluaga and R. Richards-Kortum, "Spatially resolved spectral interferometry for determination of subsurface structure.," Optics letters 24(8), 519–21 (1999).
21. L. Ginner, A. Kumar, D. Fechtig, L. M. Wurster, M. Salas, M. Pircher, and R. A. Leitgeb, "Noniterative digital aberration correction for cellular resolution retinal optical coherence tomography in vivo," Optica 4(8), 924–931 (2016).
22. V. P. Pandiyan, A. Maloney-Bertelli, J. A. Kuchenbecker, K. C. Boyle, T. Ling, Z. C. Chen, B. H. Park, A. Roorda, D. Palanker, and R. Sabesan, "The optoretinogram reveals the primary steps of phototransduction in the living human eye," Sci Adv 6(37), eabc1124 (2020).
23. L. Han, B. Tan, Z. Hosseinaee, L. K Chen, D. Hileeto and K. Bizheva, “Line-scanning SD-OCT for in-vivo, non-contact, volumetric, cellular resolution imaging of the human cornea and limbus”, Biomed. Optics Express (2022).
24. K. Neuhaus, S. Khan, O. Thaware, et al., “Real-time line-field optical coherence tomography for cellular resolution imaging of biological tissue,” Biomed. Opt. Express 15, 1059–1073 (2024).
25. K. Chen, W. Song, L. Han and K. Bizheva, “Powell Lens-based Line-Field Spectral Domain Optical Coherence Tomography system for cellular resolution imaging of biological tissue”, *Biomed. Optics Express* Vol. 14, Issue 5, pp. 2003-2014 (2023).
26. J. Lu, B. Gu, X. Wang, and Y. Zhang, “High speed adaptive optics ophthalmoscopy with an anamorphic point spread function,” Opt. Express 26(11), 14356–14374 (2018).

27. V. P. Pandiyan, X. Jiang, A. Maloney-Bertelli, J. A. Kuchenbecker, U. Sharma, and R. Sabesan, "High-speed adaptive optics line-scan OCT for cellular-resolution optoretinography," Biomed. Opt. Express 11, 5274-5296 (2020).
28. “ANSI Z80.36-2016 - Ophthalmics - Light Hazard Protection for Ophthalmic Instruments,” https://webstore.ansi.org/standards/vc%20(asc%20z80)/ansiz80362016.
29. G. S. King, “Handbook of toxicologic pathology,” Arch. Pathol. & laboratory medicine 126, 1138–1140 (2002).

Chapter 5
Line-field dynamic optical coherence tomography platform for volumetric assessment of biological tissues

5.1 Introduction

Optical Coherence Tomography (OCT) is an optical imaging modality based on low-coherence interferometry, that can generate volumetric images of biological tissues in a contactless, non-invasive way and with micrometer scale spatial resolution [1, 2]. While originally OCT was developed for morphological imaging, over the past three decades different system designs, data acquisition protocols and data processing algorithms have been developed to expand the application of OCT to mapping blood vasculature, measuring blood flow, blood oxygenation and blood glucose concentration, assessing physiological processes and mapping birefringence in biological tissues [2]. Dynamic OCT is one such example where OCT data is collected repeatedly from the imaged object over an extended period of time (from tens of seconds to several minutes) and the temporal changes in the OCT interferogram (intensity and phase) are analyzed to extract information about the motility of biological cells and their organelles [3]. The motility data can be used in several ways: as an indirect measure of the cellular metabolic and physiological processes, including apoptosis [4-9]; as a method to enhance image contrast in morphological OCT images, in order to improve the visualization of cells and their nuclei [10-13]; and as a potential method for label-free identification of cell types [10, 14, 15]. The idea of using temporal fluctuations in the OCT signal generated by light scattered from single cells to study cell apoptosis was first proposed by Van der Meer, et.al. [4]. Over the past decade, the range of biomedical applications of dOCT has expanded from imaging cell cultures and spheroids for cancer research [9, 16-18], to imaging retinal organoids for evolutionary development studies [14, 19], to ex-vivo morphological imaging of healthy and pathological tissues with enhanced contrast to visualize the tissue's cellular structure [20-22].

High-speed data acquisition is crucial if dOCT is adopted for in-vivo animal and human studies to suppress motion artifacts arising from breathing, heart rate, muscle twitching, etc. Although most published dOCT studies have been conducted ex-vivo or in-vitro in cell cultures or tissue samples, high-speed data acquisition and adequate system sensitivity are still desirable, particularly for volumetric dOCT data collection. Sufficiently high data acquisition speed could significantly reduce

the time required to collect volumetric dOCT data from hundreds of seconds to dozens of seconds or less. Accelerating data collection minimizes artifacts caused by cellular movement, tissue relaxation, and environmental vibrations. The reduced exposure time also subjects the sample to less phototoxicity and reduces inconsistencies in dynamic signal over time, which can result from prolonged exposure to environmental factors such as unsuitable temperature and humidity. One direct method to decrease data acquisition time is to increase the scanning speed of the system. Point-scanning Swept-Source OCT (SS-OCT) systems can achieve A-scan rates of several MHz [23, 24], while Full-Field Swept-Source OCT (FF-SS-OCT) systems can reach rates of several tens of MHz [25], both displaying excellent Signal-to-Noise Ratio (SNR) roll-off characteristics. However, the consequence of the high scanning speeds achieved with SS-OCT systems is reduced axial resolution and system SNR. To our knowledge, no system employing these high speeds has been directly applied on dynamic studies. In the realm of Spectral-Domain OCT (SD-OCT), a point-scanning SD-OCT system operating at 600 kHz was used recently for dOCT studies of murine liver [12]. However, the high scanning speed limited the system's SNR of 51 dB measured at a depth of 80 μm. Another high-speed Time-Domain FF-OCT (TD-FF-OCT) system was used a few years ago for a retinal organoids dOCT study [14]. This system takes advantage of the parallel data collection capability inherent to FF-OCT systems, enabling the generation of an XY (enface) direction image with a 1440×1440 resolution at a 100 Hz rate, while maintaining an adequate system SNR for dynamic signal analysis. However, the system's axial resolution was limited to ~ 13 μm in biological tissue, which reduced the differentiation of cellular structures and dynamic signals along the axial direction.

Line-Field OCT (LF-OCT) is another type of high-speed OCT imaging modality. Similar to Full-Field OCT (FF-OCT), LF-OCT also employs parallel data collection to increase data collection speed, but it does so in the XZ (B-scan) direction [26, 27]. Although numerous morphological and functional studies have utilized LF-OCT systems over the past decade [28-34], to the best of our knowledge, its application in dOCT has not yet been explored. Here, we present a novel design of a Spectral-Domain LF-dOCT (SD-LF-dOCT) system that combines high axial resolution (2.6 μm in free space, corresponding to ~ 1.9 μm in biological tissue assuming an average refractive index of 1.38), high image acquisition rate and utilizes a combination of exchangeable telecentric pair and microscope objectives to allow for FOV and transverse resolution selection.

5.2 Methods

5.2.1 LF-dOCT hardware

5.2.1.1 System design

The LF-OCT used for the volumetric dOCT studies reported here is a modified version of an LF-OCT system we reported recently [35]. Major differences in the optical design include a new camera and new design of the sample arm. Figure 5.1 shows a schematic of the novel LF-dOCT system. A superluminescent diode (cBLMD-T-850-HP, Superlum) is utilized as the system's light source. The reflective collimator (RC04APC-P01, Thorlabs) generates a collimated beam with a 3.9 mm 1/e2 intensity diameter. Although a Powell lens offers superior line-direction illumination uniformity, as discussed in our prior works [30, 35], we have opted for a cylindrical lens (CL1) as the line generator in this system to simplify the alignment process. A pair of cylindrical lenses, CL2 and CL3 are used to expand the beam in the line direction (Y direction), while leaving the beam in the scanning direction (X direction) unchanged. A 50:50 non-polarized cubic beam splitter (BS014, Thorlabs) forms the core of the free space Michelson interferometer.

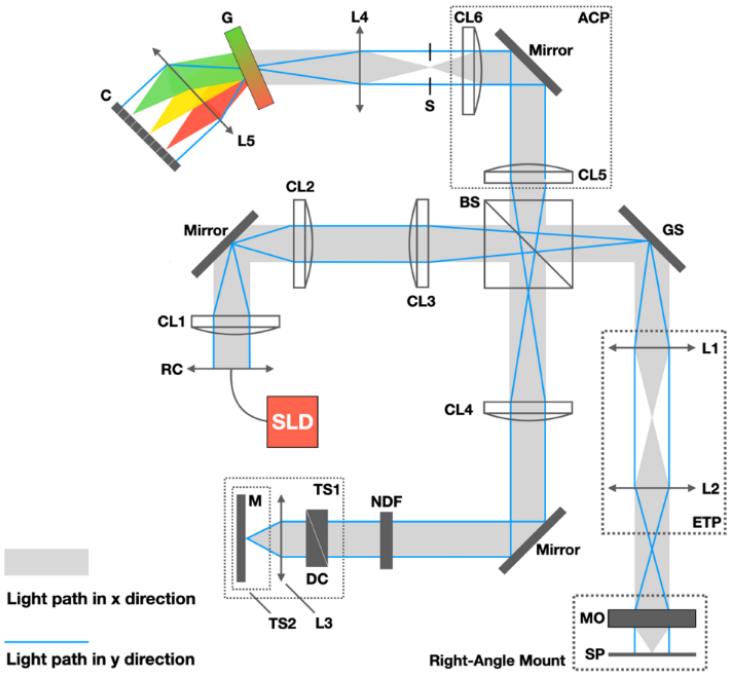

Fig. 5.1. Schematic diagram of the LF-dOCT system. SLD: superluminescent diode; RC: reflective collimator; CL: cylindrical lens; BS: beam splitter; NDF: neutral density filter; TS: translation stage;

DC: dispersion compensation unit; L1-L4: achromatic lens; GS: galvo scanner; ETP: exchangeable telecentric pair; MO: microscope objective; SP: sample plane; ACP: anamorphic cylindrical pair; S: slit; G: grating; L5: camera lens; C: camera sensor. CL1 = CL6 = 50 mm, CL2 = 150 mm, CL3 = CL4 = 100 mm, CL5 = 250 mm, L1 = L2 = 125 mm (default), L3 = 40 mm, L5 = 80 mm, L5 = 85 mm.

Compared to our previous work [35], the reference arm's layout remains unchanged; however, two modifications have been introduced to the sample arm to improve the system's imaging flexibility: an Exchangeable Telecentric Pair (ETP) design and a right-angle mount before the microscope objective. The telecentric pair lenses L1 and L2 are confined inside lens tubes with 3D printed spacers. A selection of telecentric lens pairs, each with a combined focal length of 250 mm, though different magnification power, has been pre-designed and prepared for quick exchange to allow for user choice of image FOV and transverse resolution (Fig. 5.2D). After installing a new pair onto cage plates, no further system adjustments are necessary, except for fine-tuning the position of the microscope objective and matching the dispersion between the reference and sample arms of the system. Additionally, the right-angle mount (KCB1, Thorlabs) is positioned before the microscope objective, allowing for an easy switch between vertical and horizontal imaging modes for different imaging applications.

The detection arm of the system includes an anamorphic cylindrical lens pair to facilitate separate magnification control in the X and Y directions. The spectrometer features a transmissive grating with 1200 lines per millimeter (@ 830 nm, Wasatch Photonics). The interferometric OCT signal is captured by a 2D CMOS camera (FASTCAM NOVA S9, Photron, 1024×1024 pixels) with a pixel size of 20 × 20 μm^2. The LF-dOCT system was designed so that all 1024 pixels are used in the spectral direction, while 512 pixels are used in the B-scan direction.

5.2.1.2 System performance

Figure 5.2 summarizes results from the performance test of the novel LF-dOCT system that were carried out under the following conditions: camera with a shutter speed of 2000 fps, a 10X microscopic objective (M Plan APO NIR Infinity Corrected, Mitutoyo), an incident power of approximately 3.5 mW at the image plane. Fig. 5.2A illustrates the normalized spectrum measured at the detection end of the system from reflective mirrors in the sample and reference arms. The spectrum has a full width at 179 μm, centered at 844 μm on the camera. Figure 5.2B shows the system’s axial point-spread function (PSF) measured at a depth of 100 μm. The Full Width at Half Maximum (FWHM) of the axial PSF,

measured in air, is 2.6 µm, corresponding to ~1.9 µm in biological tissues assuming an average refractive index of 1.38. Fig. 5.2C shows the system's sensitivity roll-off, with a sensitivity of 90.5 dB measured at a 100 µm depth and a 10 dB roll-off occurring at a depth of 700 µm. Fig. 5.2D provides a tabulated summary of the theoretical transverse resolutions calculated for 845 nm central wavelength for two different ETP configurations, using microscope objectives with magnifications of 5X, 10X, and 20X.

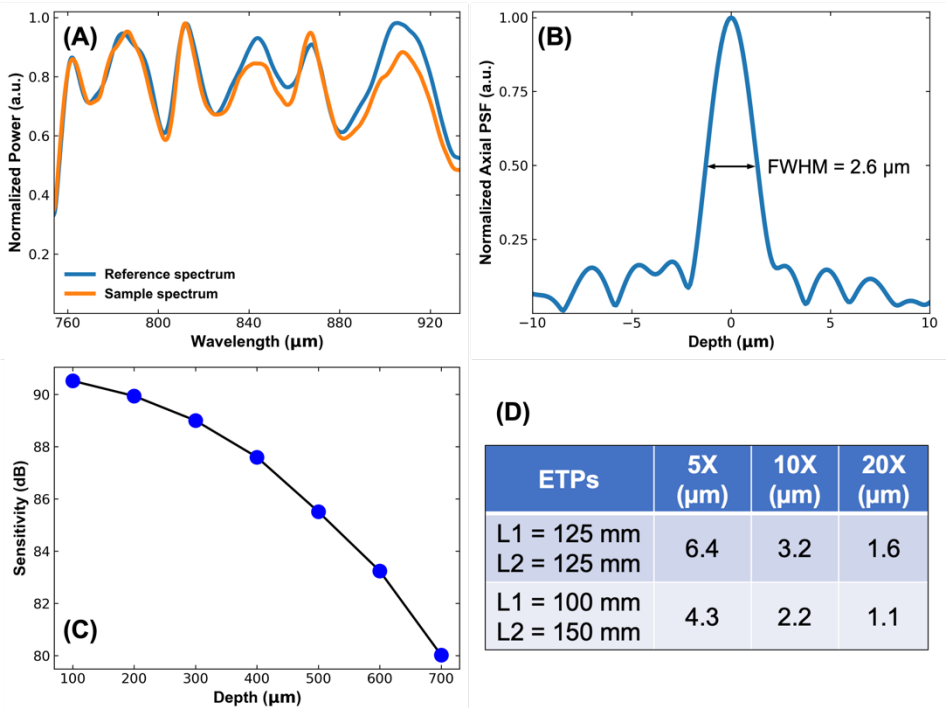

ETPs	5X (µm)	10X (µm)	20X (µm)
L1 = 125 mm L2 = 125 mm	6.4	3.2	1.6
L1 = 100 mm L2 = 150 mm	4.3	2.2	1.1

Fig. 5.2. (A) Normalized sample and reference spectra. (B) Axial PSF measured at 100 µm depth. (C) Sensitivity roll-off. (D) Theoretical LF-dOCT lateral resolutions of the for different ETPs and microscope objectives combinations.

5.2.2 dOCT Algorithm

The dOCT algorithm used in this study is based on the principle of employing FFT to isolate different cellular vibration frequencies and can be broadly divided into two main stages: the FFT operations stage, which extracts the dynamic signals, and the contrast adjustments stage, which finalizes the RGB image, as illustrated in Fig. 5.3. OCT B-scans with linearly scaled intensity captured at the same location at different time intervals are compiled into a volumetric dataset. In this context, the X and Y axes of the volume represent the standard B-scan directions, while the Z-axis corresponds to the time

direction. A Hann window function is applied along the Z-axis to mitigate sidelobe artifacts and frequency leakage due to the FFT. Zero-padding is applied at the ends of the Z-axis to improve digital resolution. An FFT is applied along the Z-axis at each voxel position, followed by logarithmic scaling of the intensity data to recalibrate the frequency amplitude distribution. Three integrals are calculated on the post-FFT frequency curve to extract distinct motion peaks for the red (slow motion), green (medium motion), and blue (fast motion) channels. The boundaries for the 3 frequency regions are dependent on the cellular dynamics of the imaged tissue samples. For this study, the RGB channels are defined as follows: red color indicates frequencies below 0.5 Hz, green color represents 0.5 to 5 Hz, and blue color signifies 5 to 12 Hz for imaging English cucumbers; for imaging mouse liver tissue, the blue color frequency range was extended up to 25 Hz; and for tumor spheroids, the blue channel was deactivated.

Although all OCT B-scans undergo the same FFT processing, in the contrast adjustment stage, it is necessary to take into account random variations in the recorded signal and background intensities. To achieve a uniform intensity distribution throughout the 3D dataset, a sample frame from near the center of the dataset is selected to establish baseline values for global background subtraction and intensity normalization. Subsequently, a predetermined contrast modification value is applied, along with a 3 × 3 median filter, to enhance image visibility. Finally, the three channels are combined to create the composite 8-bit RGB images.

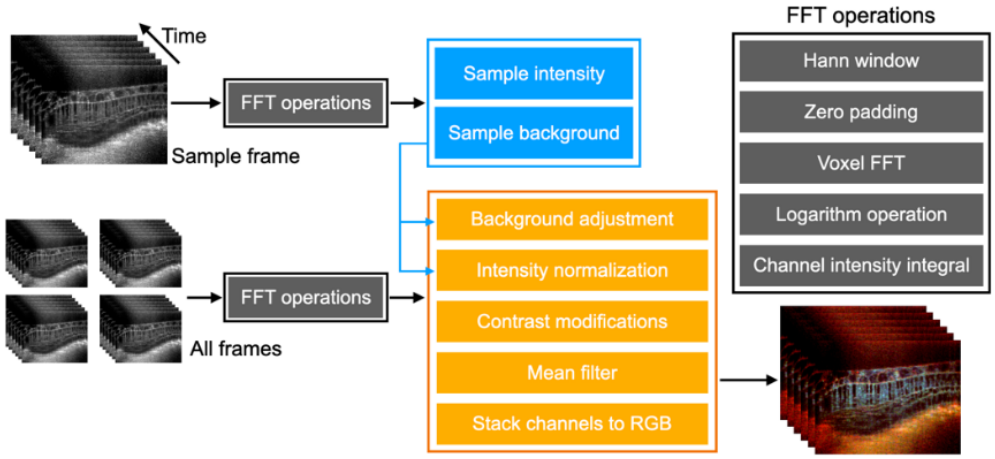

Fig. 5.3. FFT-based dOCT algorithm flow diagram.

5.2.3 Sample preparation and dOCT scanning protocols

Plant tissue (English cucumber) and animal tissue (murine liver and prostate carcinoma spheroids) were imaged with the LF-dOCT system using imaging power of ~3.5 mW. An English cucumber was sliced transversely to access the soft tissue near the seeds. This tissue contains cells ranging from ~ 10 µm to ~100 µm in diameter in a small volume. For this study, we imaged the region next to the surface of a seed, in order to demonstrate the high spatial resolution of the LF-SD-dOCT system. ETP configuration 2 with a 10X microscope objective, resulting in ~2.2 µm lateral resolution, was employed for imaging the English cucumber.

Mice (C57BL/6) were humanely euthanized and dissected to remove the liver, following an ethics protocol that was approved by the University of Waterloo Office of Research Ethics. The tissue was preserved in saline and imaged mounted in a custom sample holder placed on a 3D translation stage for imaging with the LF-SD-dOCT system. ETP configuration 1 with a 10X microscope objective, resulting in ~3.3 µm lateral resolution, was used.

Prostate carcinoma spheroids of approximately 1,000 cells were created by seeding a “3D Petri Dish” (MicroTissues Inc. USA) made of 2% agarose gel with PC3 (human, prostate, adenocarcinoma) cell line. The cells were cultured in RPMI 1640 supplemented with 10% fetal bovine serum and 1% penicillin and maintained at 37°C with 5% CO2 in a humidified atmosphere. Imaging was performed 24 hours after seeding and some spheroids were fixed with 4% formaldehyde for 1 hour immediately before imaging. The spheroids were imaged with ETP configuration 1 and a 5X microscope objective, resulting in ~6.4 µm lateral resolution.

A scanning protocol named Variable sub-Volume Multi-scan (VVMs) was developed for acquisition of volumetric LF-dOCT images from different biological tissues. The fundamental concept of VVMs is to divide the total scanning area into 'M' sub-volumes and to allocate 'N' scanning repetitions to each sub-volume. Fig. 5.4A presents a sample VVMs protocol where the total scanning volume is divided into three sub-volumes (M = 3), and two scanning repetitions are assigned to each sub-volume (N = 2). The red lines in the diagram indicate the periods of dOCT data collection, while the black lines denote the scanner's restoration time, typically set between 10% and 30% of a sub-volume duty cycle. Orange circles highlight the scanner’s non-linear behavior regions due to the abrupt change in scanning direction with high angular frequencies, which cause discontinuities in the actual dataset on the XY plane (enface) and YZ plane views. To mitigate or eliminate these discontinuities, as shown in Fig.

5.4B, the approach is to introduce additional test frames at the end of each scanning repetition. These extra frames, which extend into the subsequent scanning sub-volume, are not recorded. Fig. 5.4C shows a tabulated diagram of the protocols employed for imaging the cucumber, mouse liver, and spheroid tissues for this study.

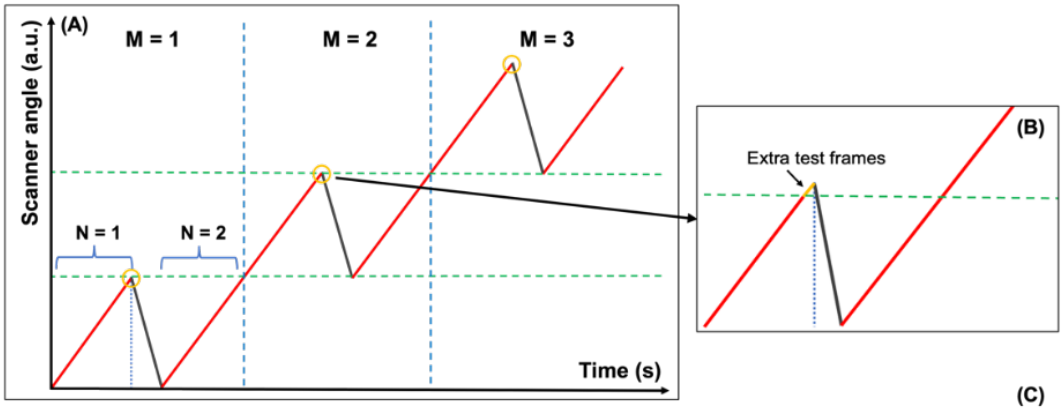

(C)

Tissue type	Camera speed [fps]	Total volume frames	Sub-volume # (M)	Sub-volume repeat rate (Hz)	Repetitions (N)	Volume collecting time (s)
English cucumber	4000	400	4	24.6	100	16.3
Murine liver	2000	200	20	129.9	260	20
Prostate cancer spheroids	2000	400	4	10.7	40	15

Fig. 5.4. (A) Scanner angle deviation with M = 3, N = 2 VVMs protocol. Orange circles correspond to the scanner non-linear behavior regions. (B) Overshot test frames to the next sub-volume for reducing the discontinuity. (C) VVMs and scanning parameters for English cucumber, mouse liver and tumor spheroids imaging.

5.3 Results

5.3.1 English cucumber

Volumetric grayscale morphological OCT and processed dOCT images of cucumber tissue acquired near the surface of a seed are shown in Figs. 5.5A and 5.5B respectively. Figs. 5.5C and 5.5D respectively show representative morphological and dOCT enface images generated from the volumetric data sets. While both the morphological and dOCT images clearly show the cellular structure of the cucumber tissue near the surface of the seed, the enhanced color contrast of the dOCT images allows for observation of morphological details in the highly scattering seed tissue.

Furthermore, the cell membranes in the dOCT images appear in blue color for the small sized cells and red color for the larger sized cells (white arrow in Fig. 5.5D), implying a difference in the cellular metabolic activity.

Similar patterns are observed in the cell nuclei: the inset in Fig. 5.5D (orange box) shows a magnified region which contains three nuclei outlined by white dashed circles. These nuclei appear in a range of mixed colors from red to green, whereas the larger nuclei, indicated by green arrows in Fig. 5.5D, predominantly exhibit a reddish hue. The red dashed box in Figs. 5.5C and 5.5D highlights the seed region. Although this region shows the highest intensity in the morphological image, it exhibits a reddish hue in the dOCT image, suggesting comparatively low metabolic activity.

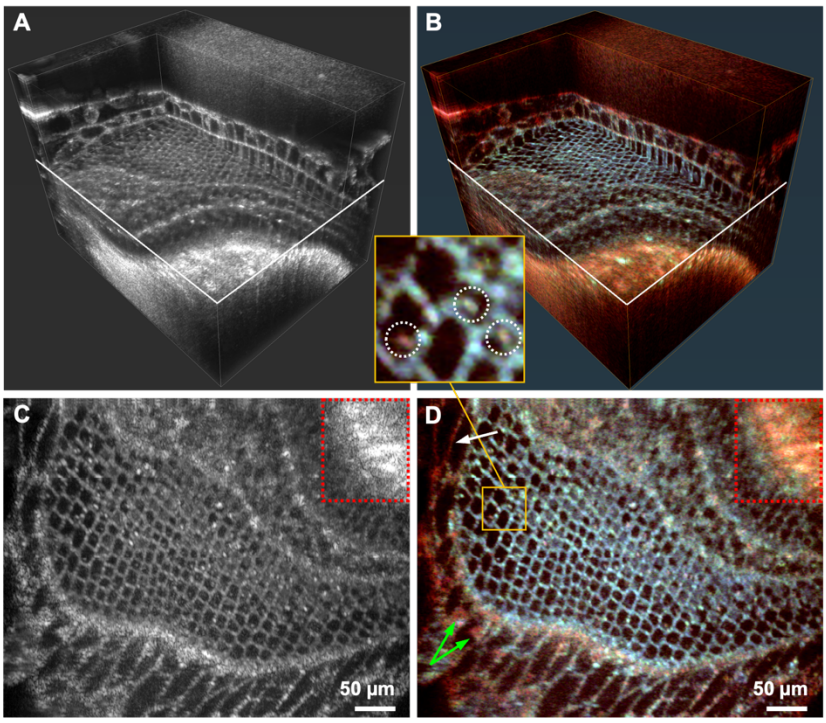

Fig. 5.5. Morphological and dOCT images of cucumber tissue. (A) Volumetric morphological OCT. (B) Volumetric dOCT. Red color: < 0.5 Hz, Green color: 0.5 – 5 Hz, Blue color: 5 – 12 Hz. (C) Enface morphological OCT with clearly visible cellular structure.. The seed region is labelled with red dashed box. (D) Same enface plane of the dOCT volume. Membrane of large cells labeled with a white arrow. Large cell nuclei and small cell nuclei are labelled with green leave arrows. Inset (orange box) region is magnified with three nuclei labelled with white dashed circle.

5.3.2 Mouse liver

Figure 5.6 shows representative images of mouse liver tissue. A volumetric dOCT image is shown Fig. 5.6A. Here, red color corresponds to frequencies below 0.5 Hz, green color to frequencies between 0.5 and 5 Hz, and blue color to frequencies between 5 and 25 Hz. Figs. 5.6B to 5.6E depict an enface plane cropped from the data in Fig. 5.6A, each utilizing different data processing methods. Fig. 5.6B reveals the averaged grayscale morphological OCT enface image with conventional OCT data processing approach. Although multiple round dark dots corresponding with nuclei positions are scattered across the frame (red arrow), when compared with the dynamically processed dataset (Figs. 5.6C-5.6E), the image lacks sufficient contrast to resolve cellular. Fig. 5.6C shows the corresponding enface image after applying time-directional standard deviation (STD) processing, which significantly enhances the image contrast compared to that in Fig. 5.6B. However, the hepatocytes are displayed with varying intensities and multiple highly reflective white spots are visible in this image, highlighting the STD method's sensitivity to anomalous values. Representative hepatocyte nuclei are marked with the red arrow. Figs. 5.6D and 5.6E show the same enface image processed with dOCT for color enhancement. Fig. 5.6D shows the standard color scheme, while Fig. 5.6E shows the tissue with a reverse color scheme (blue for frequencies below 0.5 Hz, green for 0.5 to 5 Hz, and red for 5 to 25 Hz). Both individual hepatocytes and their nuclei are clearly visible in the two dOCT images.

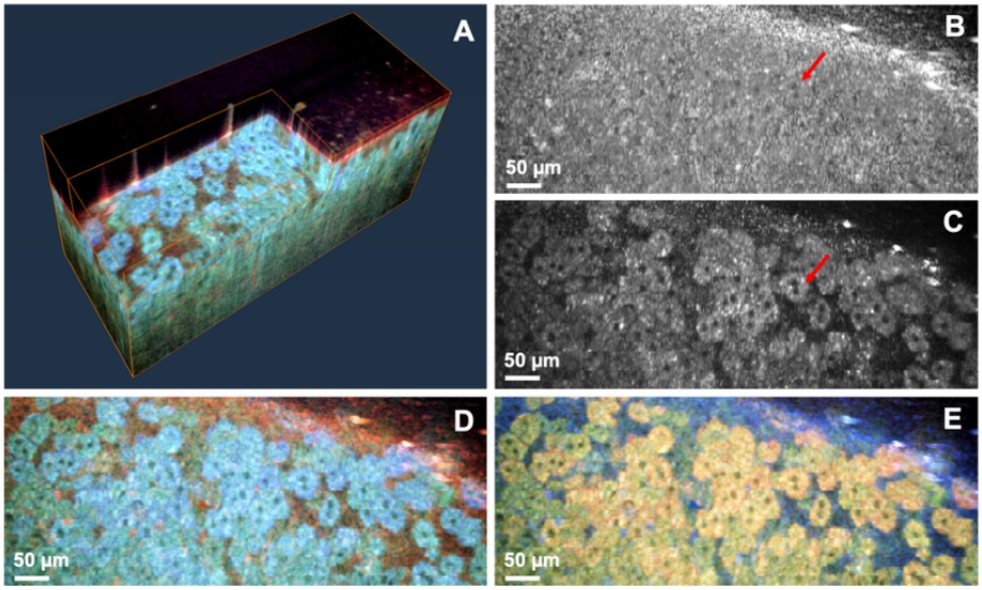

Fig. 5.6. OCT and dOCT images of mouse liver. (A) Volumetric dOCT image. Red color: < 0.5 Hz, green color: 0.5 – 5 Hz, and blue color: 5 – 25 Hz. (B) Grayscale morphological OCT enface view of

the liver tissue. Dark dots correspond to cellular nuclei (red arrow). (C) Grayscale enface view of the liver tissue enhanced by the standard deviation processing of the raw data. Individual cells are clearly visible. Dark dots correspond to cellular nuclei (red arrow). (D) Enface view of the liver tissue enhanced by the dOCT method. (E) The same dOCT-enhanced enface view of the liver tissue with reversed color channel distributions: blue color: < 0.5 Hz, green color: 0.5 – 5 Hz, and red color: 5 – 25 Hz.

5.3.3 Prostate carcinoma spheroids

Volumetric and enface grayscale morphological OCT images of prostate carcinoma spheroids are shown in Figs. 5.7A and 5.7B respectively. Figs. 5.7C and 5.7D depict dOCT enface images of a live spheroid (control) and a spheroid that has been fixed respectively. The agarose gel in which the spheroids are cultured has been removed from the dOCT enface images.

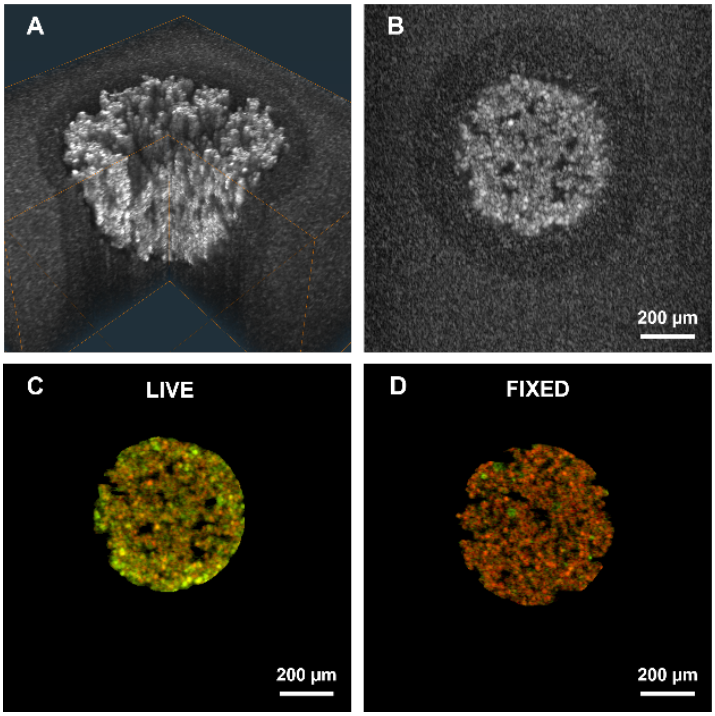

Fig. 5.7. OCT and dOCT images of prostate carcinoma spheroids. (A) Volumetric grayscale morphological OCT image of a live prostate carcinoma spheroid. (B) Grayscale morphological OCT enface view of the same live prostate carcinoma spheroid. (C) Enface view of the same live prostate carcinoma spheroid enhanced with dOCT. (D) Enface view of a prostate carcinoma spheroid fixed with 4% formaldehyde enhanced with dOCT. Red color: < 0.5 Hz, and green color: 0.5 – 5 Hz.

Here, the blue frequency band was not used, but as in the liver tissue, red color corresponds to frequencies below 0.5 Hz and green color to frequencies between 0.5 and 5 Hz. Cells in the dOCT images appear in a range of mixed colors from red to green, with live cells appearing largely in green and yellow color (Fig. 5.7C) and cells in the fixed prostate carcinoma spheroid predominantly exhibiting a reddish hue (Fig. 5.7D).

5.4 Discussion

The dOCT results for cucumber (Fig. 5.5), mouse liver (Fig. 5.6), and prostate carcinoma spheroids (Fig. 5.7) showcase the capabilities of the LF-dOCT platform. For the cucumber, although there are no direct dOCT comparative studies, the outcomes align with general expectations and are consistent with findings from research on the metabolic behaviors of plant cells [36]. In Fig. 5.5D, smaller cells indicative of recent differentiation typically exhibit higher metabolic signals, so their membranes appear blue. Conversely, cells that are larger, more mature, and located farther from the seed's surface display membranes with a more reddish hue, corresponding to lower metabolic activity as expected. The nuclei of these smaller cells in Fig. 5.5D exhibit a spectrum of colors from red to blue. The larger cell nuclei, indicated by green arrows, mainly present a reddish hue, suggesting either reduced metabolic activity or that the large nuclei inertia prevents vibrations. The red dashed box in Figs. 5.5C and 5.5D identifies the cucumber seed region. Despite its high-intensity signal in the morphological plot, it demonstrates limited hues within high-frequency ranges and does not appear as the brightest region in the dOCT plot. This implies that the dOCT algorithm utilized for this study prioritizes signal variations over absolute intensities. Beyond color differentiation, the dOCT algorithm also accentuates structures that are not distinctly visible in grayscale images. For example, multiple small cells in the central and right regions of Fig. 5.5C exhibit membranes that are not clearly defined, yet these same cells appear with sharp boundaries in Fig. 5.5D.

The mouse liver tissue analysis demonstrates that both the STD and FFT dOCT techniques can effectively distinguish hepatocytes from their surrounding environment, as depicted in Figs. 5.6C to 5.6E. Since STD can be affected by anomalous values leading to biased readings, the bright spots and the varying intensities on either side of the plot in Fig. 5.6C are likely artifacts of this limitation. In contrast, the dOCT algorithm employed in this study, despite requiring a more intensive computational effort, yields a more uniform distribution of hues and intensities throughout the image. When similar frequency bands and color channels are selected, Fig. 5.6E displays morphology and hues of

hepatocytes that closely align with those found in other dOCT studies on murine liver performed with point-scanning SD-OCT, despite differences in the spatial resolution, image acquisition rate and scanning protocols [10, 12].

Analysis of the prostate carcinoma spheroids demonstrates that the FFT dOCT technique is capable of discerning live spheroids from those that have been fixed with formaldehyde. Live prostate carcinoma spheroids appear predominantly green in color, whereas fixed spheroids appear largely in red color. The fixation process causes cellular apoptosis and therefore eliminates any cellular metabolic activity while maintaining the structure of the spheroid in the short time frame this study was conducted, which suggests that the increased green color present in live spheroids is due to metabolic processes driven by ATP consumption. A reduced spectral density at higher frequencies observed in the fixed cells has also been observed in mammary epithelial cells within organoids and was suggested to represent more Brownian like motion [9]. We hypothesize that Brownian motion may be the cause of the few fixed cells that do appear green in color, as the spheroids are suspended in culture medium.

Several factors related to potential limitations and improvements of the system's hardware and algorithms are discussed separately in the following subsections.

5.4.1 System sensitivity

The current design of the LF-dOCT system achieves a maximum sensitivity of 90.5 dB for data acquisition rate of 2,000 fps and optical power of 3.5 mW incident on the tissue surface. This limits acquisition of volumetric dOCT images at imaging depths > 500 μm within highly scattering biological tissues such as skin, liver, etc. One approach to improving the system’s sensitivity is to increase the incident optical power on the sample’s surface; however, since the SLD utilized in the current version of the LF-dOCT system is already operating at its maximum (15 mW), further increments would require changing the light source. Potentially doubling the incident power while maintaining a similar light source relative intensity noise (RIN) could improve the system’s sensitivity by 3 dB. However, this approach will increase phototoxicity, especially for light-sensitive tissues such as retina and retinal organoids [14, 37] and may pose safety concerns for potential in-vivo ocular studies in animals and humans. Supercontinuum based light sources offer much more powerful output, though their RIN is significantly higher, therefore this approach offers very limited improvement in the LF-dOCT sensitivity.

Another approach is to replace the 50:50 beam splitter in the current LF-dOCT design with a 70:30 beam splitter, which should result in ~1dB sensitivity improvement. Another advantage of this approach will be reduced phototoxicity for the imaged biological tissue.

A third approach would require reducing the camera data acquisition rate. While this approach might be generally feasible, it is dependent on the camera dynamic range. The Photron camera used in the current version of the LF-dOCT system has been designed for high sensitivity to very low light levels, therefore it is easily saturated by specular reflections from optical components in the system and from the air-tissue interface. The current limitation of the LF-dOCT system when reducing the camera acquisition rate to below 1,000 fps is the inability to completely block on-axis or near-on-axis reflections from optics in the sample arm, which currently constitute less than 5% of the camera's saturation level. Potential solutions to this issue include adjusting the orientations of the lens pair L1 and L2 relative to the Y-axis, which could help reduce reflections [32], or replacing the lens pair with mirrors.

5.4.2 Data processing and analyzing

The processing codes for both OCT and dOCT in this study are written in Python, utilizing the NumPy package for parallel array operations and the multiprocessing package for multi-threaded processing. The data processing is performed on a personal computer (CPU: AMD 7950X; RAM: 64 GB DDR5; storage: SN850X 4TB; operating system: Windows 10). At 100% CPU usage, processing a dataset with 200 B-scan locations and 260 repetitions per B-scan location (as per the murine liver protocol) takes 90 seconds for OCT and 43 seconds for dOCT data sets. The OCT processing takes roughly twice as long due to the tasks involved in writing the post-FFT datasets to storage. Given that the NumPy package is built using C and C++, and most computational tasks within the processing code are managed by NumPy functions, migrating the code from Python to C++ may not result in a significant increase in processing speed. Conversely, the existing code does not utilize GPU acceleration. Incorporating a GPU-based FFT package, such as CuPy, could expedite processing, especially with large-sized arrays. While the computational requirements of existing protocols preclude real-time display of volumetric dOCT datasets, a real-time display of a single B-scan location dOCT view could be readily achieved using the LF-dOCT system, as it requires only tens of frame exposures per second.

The system can theoretically detect a maximum dynamic frequency equal to half of the sub-volume repeat rate, as dictated by the Nyquist-Shannon sampling theorem [38]. In the analysis of cucumber

dOCT, the upper dynamic frequency threshold is set at 12 Hz, which nearly reaches the theoretical limit. Conversely, for mouse liver tissue dOCT analysis, the upper dynamic frequency limit is established at 25 Hz, aligning with other dynamic studies on liver tissues, despite the protocol supporting a theoretical limit of approximately 65 Hz. Prostate carcinoma spheroids employed an upper dynamic frequency limit of 5 Hz, which was sufficient to distinguish metabolically active live spheroids from metabolically dead fixed spheroids. During imaging sessions, it was observed that for more transparent tissues, such as cucumber slices, the extraction and analysis of dynamic signals near the upper frequency limit could be carried out with considerable accuracy. However, this accuracy decreases with an increase of the tissue's optical density. Consequently, a denser scanning protocol has been devised for liver tissue to enhance accuracy.

5.4.3 Future work

Looking ahead, the LF-dOCT platform's versatile ETP design, when paired with microscope objectives of varying magnifications, promises a lateral resolution spectrum ranging from approximately 1 μm to 6.5 μm. Such flexibility is poised to enable a diverse array of studies, from single-cell metabolic activity to intracellular interactions within cellular clusters. Future developments include refining algorithms to correct motion artifacts, which will enhance the platform's utility for in-vivo dOCT ocular studies on animals such as those with limbal stem cell dysfunction. Additionally, there is potential for altering scanning protocols and dOCT algorithms to allow for real-time visualization of volumetric dOCT datasets. The platform's free-space design also offers the possibility of incorporating supplementary imaging modalities, such as fluorescence microscopy and other OCT techniques like Full-Field OCT, thereby paving the way for a multifaceted imaging system.

5.5 Conclusion

In conclusion, we have developed an LF-dOCT platform that allows for acquisition of volumetric dOCT images and offers considerable flexibility in adjusting the lateral resolution as necessary for different biomedical imaging applications. We have demonstrated cellular resolution dOCT imaging in different biological tissues (cucumber and mouse liver). By leveraging the high-speed capabilities of LF-OCT, we have managed to reduce the acquisition time for a volumetric dOCT dataset to under one minute. We plan to use this platform for a range of future in-vitro and in-vivo studies, from observing single-cell metabolic behaviors to investigating intracellular interactions.

5.6 References

1. D. Huang, E. A. Swanson, C. P. Lin, et al., “Optical coherence tomography,” science 254, 1178–1181 (1991).
2. W. Drexler and J. G. Fujimoto, eds., Optical Coherence Tomography, 2nd ed. (Springer, 2015).
3. S. Azzollini, T. Monfort, O. Thouvenin, and K. Grieve, “Dynamic optical coherence tomography for cell analysis,” Biomed. optics express 14, 3362–3379 (2023).
4. F. J. van der Meer, D. J. Faber, M. C. Aalders, et al., “Apoptosis-and necrosis-induced changes in light attenuation measured by optical coherence tomography,” Lasers medical science 25, 259–267 (2010).
5. C. Apelian, F. Harms, O. Thouvenin, and A. C. Boccara, “Dynamic full field optical coherence tomography: subcellular metabolic contrast revealed in tissues by interferometric signals temporal analysis,” Biomed. optics express 7, 1511–1524 (2016).
6. C.-E. Leroux, F. Bertillot, O. Thouvenin, and A.-C. Boccara, “Intracellular dynamics measurements with full field optical coherence tomography suggest hindering effect of actomyosin contractility on organelle transport,” Biomed. Opt. Express 7, 4501–4513 (2016).
7. S. Park, T. Nguyen, E. Benoit, et al., “Quantitative evaluation of the dynamic activity of hela cells in different viability states using dynamic full-field optical coherence microscopy,” Biomed. Opt. Express 12, 6431–6441 (2021).
8. S. Park, V. Veluvolu, W. S. Martin, et al., “Label-free, non-invasive, and repeatable cell viability bioassay using dynamic full-field optical coherence microscopy and supervised machine learning,” Biomed. Opt. Express 13, 3187–3194 (2022).
9. A. L. Oldenburg, X. Yu, T. Gilliss, et al., “Inverse-power-law behavior of cellular motility reveals stromal–epithelial cell interactions in 3d co-culture by oct fluctuation spectroscopy,” Optica 2, 877–885 (2015).
10. M. Münter, M. Vom Endt, M. Pieper, et al., “Dynamic contrast in scanning microscopic oct,” Opt. letters 45, 4766–4769 (2020).
11. G. Musial, T. Kohlfaerber, M. Ahrens, et al., “Dynamic contrast microscopic optical coherence tomography as a novel method for assessing corneal epithelium during exposure to benzalkonium chloride,” Transl. Vis. Sci. & Technol. 11, 28–28 (2022).

12. M. Münter, M. Pieper, T. Kohlfaerber, et al., “Microscopic optical coherence tomography (moct) at 600 khz for 4d volumetric imaging and dynamic contrast,” Biomed. Opt. Express 12, 6024–6039 (2021).
13. H. M. Leung, M. L. Wang, H. Osman, et al., “Imaging intracellular motion with dynamic micro-optical coherence tomography,” Biomed. Opt. Express 11, 2768–2778 (2020).
14. J. Scholler, K. Groux, O. Goureau, et al., “Dynamic full-field optical coherence tomography: 3d live-imaging of retinal organoids,” Light. Sci. & Appl. 9, 140 (2020).
15. O. Thouvenin, C. Boccara, M. Fink, et al., “Cell motility as contrast agent in retinal explant imaging with full-field optical coherence tomography,” Investig. ophthalmology & visual science 58, 4605–4615 (2017).
16. I. Abd El-Sadek, A. Miyazawa, L.W. Shen, et al., “Optical coherence tomography-based tissue dynamics imaging for longitudinal and drug response evaluation of tumor spheroids,” Biomed. Opt. Express 11, 6231 (2020).
17. I. Abd El-Sadek, A. Miyazawa, L. T.-W. Shen, et al., “Three-dimensional dynamics optical coherence tomography for tumor spheroid evaluation,” Biomed. optics express 12, 6844–6863 (2021).
18. H. Yang, S. Zhang, P. Liu, et al., “Use of high-resolution full-field optical coherence tomography and dynamic cell imaging for rapid intraoperative diagnosis during breast cancer surgery,” Cancer 126, 3847–3856 (2020).
19. T. Monfort, S. Azzollini, J. Brogard, et al., “Dynamic full-field optical coherence tomography module adapted to commercial microscopes allows longitudinal in vitro cell culture study,” Commun. Biol. 6, 992 (2023).
20. T. Kohlfaerber, M. Pieper, M. Münter, et al., “Dynamic microscopic optical coherence tomography to visualize the morphological and functional micro-anatomy of the airways,” Biomed. Opt. Express 13, 3211–3223 (2022).
21. P. Mukherjee, S. Fukuda, D. Lukmanto, et al., “Label-free metabolic imaging of non-alcoholic-fatty-liver-disease (nafld) liver by volumetric dynamic optical coherence tomography,” Biomed. Opt. Express 13, 4071 (2022).
22. R. Morishita, T. Suzuki, P. Mukherjee, et al., “Label-free intratissue activity imaging of alveolar organoids with dynamic optical coherence tomography,” Biomed. Opt. Express 14, 2333–2351 (2023).

23. W. Wieser, B. R. Biedermann, T. Klein, et al., “Multi-megahertz oct: High quality 3d imaging at 20 million a-scans and 4.5 gvoxels per second,” Opt. express 18, 14685–14704 (2010).
24. T. Klein, W. Wieser, L. Reznicek, et al., “Multi-mhz retinal oct,” Biomed. optics express 4, 1890–1908 (2013).
25. D. Hillmann, H. Spahr, C. Hain, et al., “Aberration-free volumetric high-speed imaging of in vivo retina,” Sci. reports 6, 35209 (2016).
26. T. Endo, Y. Yasuno, S. Makita, et al., “Profilometry with line-field fourier-domain interferometry,” Opt. express 13, 695–701 (2005).
27. B. Grajciar, M. Pircher, A. F. Fercher, and R. A. Leitgeb, “Parallel fourier domain optical coherence tomography for in vivo measurement of the human eye,” Opt. Express 13, 1131–1137 (2005).
28. D. J. Fechtig, B. Grajciar, T. Schmoll, et al., “Line-field parallel swept source mhz oct for structural and functional retinal imaging,” Biomed. optics express 6, 716–735 (2015).
29. L. Han, B. Tan, Z. Hosseinaee, et al., “Line-scanning sd-oct for in-vivo, non-contact, volumetric, cellular resolution imaging of the human cornea and limbus,” Biomed. Opt. Express 13, 4007–4020 (2022).
30. K. Chen, W. Song, L. Han, and K. Bizheva, “Powell lens-based line-field spectral domain optical coherence tomography system for cellular resolution imaging of biological tissue,” Biomed. Opt. Express 14, 2003 (2023).
31. V. P. Pandiyan, X. Jiang, A. Maloney-Bertelli, et al., “High-speed adaptive optics line-scan oct for cellular-resolution optoretinography,” Biomed. optics express 11, 5274–5296 (2020).
32. X. Jiang, T. Liu, V. P. Pandiyan, et al., “Coarse-scale optoretinography (coorg) with extended field-of-view for normative characterization,” Biomed. Opt. Express 13, 5989–6002 (2022).
33. Z. Zhang, X. Yang, Z. Zhao, et al., “Rapid imaging and product screening with low-cost line-field fourier domain optical coherence tomography,” Sci. reports 13, 10809 (2023).
34. K. Neuhaus, S. Khan, O. Thaware, et al., “Real-time line-field optical coherence tomography for cellular resolution imaging of biological tissue,” Biomed. Opt. Express 15, 1059–1073 (2024).
35. K. Chen, N. FIROOZJAH, A. Wong, and K. Bizheva, “Powell lens-based line-field oct for in-vivo, contact-less, cellular resolution imaging of the human cornea,” (2024).
36. D. Rontein, M. Dieuaide-Noubhani, E. J. Dufourc, et al., “The metabolic architecture of plant cells: stability of central metabolism and flexibility of anabolic pathways during the growth cycle of tomato cells,” J. Biol. Chem. 277, 43948–43960 (2002).

37. P. Zhang, O. Vafaeva, C. Dolf, et al., “Evaluating the performance of oct in assessing static and potential dynamic properties of the retinal ganglion cells and nerve fiber bundles in the living mouse eye,” Biomed. Opt. Express 14, 6422–6441 (2023).
38. A. J. Jerri, “The shannon sampling theorem—its various extensions and applications: A tutorial review,” Proc. IEEE 65, 1565–1596 (1977).

Chapter 6
Conclusion

The three main objectives of this thesis research are: (i) to investigate the performance of a Powell lens as a replacement for a cylindrical lens as the line generator for OCT imaging, (ii) to optimize the Powell lens-based OCT system for in vivo human corneal studies, and (iii) to develop a dOCT imaging platform for the assessment of various biological tissues. Generally speaking, all three goals have been achieved with the development of the first-generation PL-LF-SD-OCT system, the second-generation PL-LF-SD-OCT system, and the LF-dOCT system.

The first-generation PL-LF-SD-OCT system, which utilizes a Powell lens instead of a cylindrical lens as the line generator, was developed. This design resulted in significantly improved uniformity of illumination along the line direction and only approximately 1.6 dB sensitivity loss between the B-scan's center and edges. The system's high spatial resolution allowed for imaging the cellular structure of plant tissues and the animal cornea, as well as resolving small morphological features such as cellular nuclei in endothelial cells.

The second generation of the PL-LF-SD-OCT system improved sensitivity offered a larger FOV, and demonstrated the system's suitability for in vivo, contactless, volumetric imaging of the human cornea. Healthy corneal images acquired with this system showed that the combination of high spatial resolution, fast image acquisition rate, and improved sensitivity are sufficient to visualize individual cells and cellular nuclei in the high-contrast PL-LF-SD-OCT images, as well as to carry out morphometric analysis on the thin corneal layers, including the endothelium, Descemet's membrane, pre-Descemet's layer, and Bowman's membrane.

Finally, the development of the LF-dOCT platform allows for the acquisition of volumetric dOCT images and offers considerable flexibility in adjusting the lateral resolution as necessary for different biomedical imaging applications. We have demonstrated dOCT imaging in various biological tissues, including cucumber, mouse liver and tumor spheroids. By leveraging the high-speed capabilities of LF-OCT, we have reduced the acquisition time for a volumetric dOCT dataset to under one minute.

References

1. J. H. Krachmer, M. J. Mannis, and E. J. Holland, Cornea e-book (Elsevier Health Sciences, 2010).
2. Y. S. Rabinowitz, “Keratoconus,” Surv. ophthalmology 42, 297–319 (1998).
3. S. E. Wilson and W. M. Bourne, “Fuchs’ dystrophy,” Cornea 7, 2–18 (1988).
4. R. H. Silverman, “High-resolution ultrasound imaging of the eye–a review,” Clin. & experimental ophthalmology 37, 54–67 (2009).
5. C. Mazzotta, F. Hafezi, G. Kymionis, et al., “In vivo confocal microscopy after corneal collagen crosslinking,” The ocular surface 13, 298–314 (2015).
6. A. Labbé, P. Niaudet, C. Loirat, et al., “In vivo confocal microscopy and anterior segment optical coherence tomography analysis of the cornea in nephropathic cystinosis,” Ophthalmology 116, 870–876 (2009).
7. W. Drexler and J. G. Fujimoto, eds., Optical Coherence Tomography, 2nd ed. (Springer, 2015).
8. D. Huang, E. A. Swanson, C. P. Lin, et al., “Optical coherence tomography,” science 254, 1178–1181 (1991).
9. T. Endo, Y. Yasuno, S. Makita, et al., “Profilometry with line-field fourier-domain interferometry,” Opt. express 13, 695–701 (2005).
10. B. Grajciar, M. Pircher, A. F. Fercher, and R. A. Leitgeb, “Parallel fourier domain optical coherence tomography for in vivo measurement of the human eye,” Opt. Express 13, 1131–1137 (2005).
11. Y. Yasuno, T. Endo, S. Makita, et al., “Three-dimensional line-field fourier domain optical coherence tomography for in vivo dermatological investigation,” J. biomedical optics 11, 014014–014014 (2006).
12. D. J. Fechtig, B. Grajciar, T. Schmoll, et al., “Line-field parallel swept source mhz oct for structural and functional retinal imaging,” Biomed. optics express 6, 716–735 (2015).
13. V. P. Pandiyan, X. Jiang, A. Maloney-Bertelli, et al., “High-speed adaptive optics line-scan oct for cellular-resolution optoretinography,” Biomed. optics express 11, 5274–5296 (2020).

14. L. Han, B. Tan, Z. Hosseinaee, et al., “Line-scanning sd-oct for in-vivo, non-contact, volumetric, cellular resolution imaging of the human cornea and limbus,” Biomed. Opt. Express 13, 4007–4020 (2022).

15. N. Ehlers and J. Hjortdal, “Corneal thickness: measurement and implications,” Exp. eye research 78, 543–548 (2004).

16. D.W. DelMonte and T. Kim, "Anatomy and physiology of the cornea," Journal of Cataract & Refractive Surgery 37(3), 588-598 (2011).

17. Y. Ruan, S. Jiang, A. Musayeva, et al., “Corneal epithelial stem cells–physiology, pathophysiology and therapeutic options,” Cells 10, 2302 (2021).

18. B.H. Jeng, "Treating the nonhealing epithelial defect," CRST Europe Sept. 25-28 (2011).

19. D. L. Stocum, Regenerative biology and medicine (Academic Press, 2012).

20. D. Z. Reinstein, T. J. Archer, M. Gobbe, et al., “Epithelial thickness in the normal cornea: three-dimensional display with very high frequency ultrasound,” J. refractive surgery (Thorofare, NJ: 1995) 24, 571 (2008).

21. S. E. Wilson, “Bowman’s layer in the cornea–structure and function and regeneration,” Exp. eye research 195, 108033 (2020).

22. J. Germundsson, G. Karanis, P. Fagerholm, and N. Lagali, “Age-related thinning of bowman’s layer in the human cornea in vivo,” Investig. ophthalmology & visual science 54, 6143–6149 (2013).

23. M. S. Sridhar, "Anatomy of cornea and ocular surface.," Indian journal of ophthalmology 66(2), 190–194 (2018).

24. J. V. Jester, “Corneal crystallins and the development of cellular transparency,” in Seminars in cell & developmental biology, vol. 19 (Elsevier, 2008), pp. 82–93.

25. S. V. Patel, J. W. McLaren, D. O. Hodge, and W. M. Bourne, “Normal human keratocyte density and corneal thickness measurement by using confocal microscopy in vivo,” Investig. ophthalmology & visual science 42, 333–339 (2001).

26. J. C. Erie, S. V. Patel, J. W. McLaren, et al., “Keratocyte density in keratoconus. a confocal microscopy study,” Am. journal ophthalmology 134, 689–695 (2002).

27. H. S. Dua, L. A. Faraj, D. G. Said, et al., “Human corneal anatomy redefined: a novel pre-descemet’s layer (dua’s layer),” Ophthalmology 120, 1778–1785 (2013).

28. K. Bizheva, L. Haines, E. Mason, et al., “In vivo imaging and morphometry of the human pre-descemet’s layer and endothelium with ultrahigh-resolution optical coherence tomography,” Investig. ophthalmology & visual science 57, 2782–2787 (2016).

29. H. S. Dua, R. Freitas, I. Mohammed, et al., “The pre-descemet’s layer (dua’s layer, also known as the dua-fine layer and the pre-posterior limiting lamina layer): Discovery, characterisation, clinical and surgical applications, and the controversy,” Prog. Retin. Eye Res. 97, 101161 (2023).

30. S. Tuft and D. Coster, “The corneal endothelium,” Eye 4, 389–424 (1990).

31. Galgauskas S, Norvydaitė D, Krasauskaitė D, Stech S, Ašoklis RS. Age-related changes in corneal thickness and endothelial characteristics. Clin Interv Aging. (2013).

32. R. Leitgeb, C. K. Hitzenberger, and A. F. Fercher, "Performance of fourier domain vs. time domain optical coherence tomography," Opt. Express 11, 889-894 (2003).

33. Michael A. Choma, Marinko V. Sarunic, Changhuei Yang, and Joseph A. Izatt, "Sensitivity advantage of swept source and Fourier domain optical coherence tomography," Opt. Express 11, 2183-2189 (2003).

34. R. A. Leitgeb, W. Drexler, A. Unterhuber, B. Hermann, T. Bajraszewski, T. Le, A. Stingl, and A. F. Fercher, "Ultrahigh resolution Fourier domain optical coherence tomography," Opt. Express 12, 2156-2165 (2004).

35. Michael Münter, Mario Pieper, Tabea Kohlfaerber, Ernst Bodenstorfer, Martin Ahrens, Christian Winter, Robert Huber, Peter König, Gereon Hüttmann, and Hinnerk Schulz-Hildebrandt, "Microscopic optical coherence tomography (mOCT) at 600 kHz for 4D volumetric imaging and dynamic contrast," Biomed. Opt. Express 12, 6024-6039 (2021).

36. W. Wieser, B. R. Biedermann, T. Klein, et al., “Multi-megahertz oct: High quality 3d imaging at 20 million a-scans and 4.5 gvoxels per second,” Opt. express 18, 14685–14704 (2010).

37. A. Zuluaga and R. Richards-Kortum, "Spatially resolved spectral interferometry for determination of subsurface structure.," Optics letters 24(8), 519–21 (1999).

38. Vimal Prabhu Pandiyan, Xiaoyun Jiang, James A. Kuchenbecker, and Ramkumar Sabesan, "Reflective mirror-based line-scan adaptive optics OCT for imaging retinal structure and function," Biomed. Opt. Express 12, 5865-5880 (2021).

39. Z. Zhang, X. Yang, Z. Zhao, et al., “Rapid imaging and product screening with low-cost line-field fourier domain optical coherence tomography,” Sci. reports 13, 10809 (2023).

40. Kai Neuhaus, Shanjida Khan, Omkar Thaware, Shuibin Ni, Mini Aga, Yali Jia, Travis Redd, Siyu Chen, David Huang, and Yifan Jian, "Real-time line-field optical coherence tomography for cellular resolution imaging of biological tissue," Biomed. Opt. Express 15, 1059-1073 (2024).

41. B. Považay, A. Unterhuber, B. Hermann, H. Sattmann, H. Arthaber, and W. Drexler, "Full-field time-encoded frequency-domain optical coherence tomography," Opt Express 14(17), 7661 (2006).

42. J. Kalkman et al., “Fourier-domain optical coherence tomography signal analysis and numerical modeling,” Int. J. Opt. 2017 (2017).

43. M. Münter, M. Vom Endt, M. Pieper, et al., “Dynamic contrast in scanning microscopic oct,” Opt. letters 45, 4766–4769 (2020).

44. C. Apelian, C. Gastaud, and A. C. Boccara, “Extracting relevant information for cancer diagnosis from dynamic full field oct through image processing and learning,” in Optical Coherence Tomography and Coherence Domain Optical Methods in Biomedicine XXI, vol. 10053 (SPIE, 2017), pp. 102–108.

45. G. Musial, T. Kohlfaerber, M. Ahrens, et al., “Dynamic contrast microscopic optical coherence tomography as a novel method for assessing corneal epithelium during exposure to benzalkonium chloride,” Transl. Vis. Sci. & Technol. 11, 28–28 (2022).

46. T. Monfort, S. Azzollini, J. Brogard, et al., “Dynamic full-field optical coherence tomography module adapted to commercial microscopes allows longitudinal in vitro cell culture study,” Commun. Biol. 6, 992 (2023).

47. O. Thouvenin, C. Boccara, M. Fink, et al., “Cell motility as contrast agent in retinal explant imaging with full-field optical coherence tomography,” Investig. ophthalmology & visual science 58, 4605–4615 (2017).

48. I. Abd El-Sadek, A. Miyazawa, L. T.-W. Shen, et al., “Three-dimensional dynamics optical coherence tomography for tumor spheroid evaluation,” Biomed. optics express 12, 6844–6863 (2021).

49. I. Abd El-Sadek, A. Miyazawa, L. T.-W. Shen, et al., “Optical coherence tomography-based tissue dynamics imaging for longitudinal and drug response evaluation of tumor spheroids,” Biomed. Opt. Express 11, 6231–6248 (2020).

50. P. Mukherjee, S. Fukuda, D. Lukmanto, et al., “Label-free metabolic imaging of non-alcoholic-fatty-liver-disease (nafld) liver by volumetric dynamic optical coherence tomography,” Biomed. Opt. Express 13, 4071–4086 (2022).

51. R. Morishita, T. Suzuki, P. Mukherjee, et al., “Label-free intratissue activity imaging of alveolar organoids with dynamic optical coherence tomography,” Biomed. Opt. Express 14, 2333–2351 (2023).

52. H. M. Leung, M. L. Wang, H. Osman, et al., “Imaging intracellular motion with dynamic micro-optical coherence tomography,” Biomed. Opt. Express 11, 2768–2778 (2020).

53. T. Kohlfaerber, M. Pieper, M. Münter, et al., “Dynamic microscopic optical coherence tomography to visualize the morphological and functional micro-anatomy of the airways,” Biomed. Opt. Express 13, 3211–3223 (2022).

54. A. L. Oldenburg, X. Yu, T. Gilliss, et al., “Inverse-power-law behavior of cellular motility reveals stromal–epithelial cell interactions in 3d co-culture by oct fluctuation spectroscopy,” Optica 2, 877–885 (2015).

55. J. Scholler, K. Groux, O. Goureau, et al., “Dynamic full-field optical coherence tomography: 3d live-imaging of retinal organoids,” Light. Sci. & Appl. 9, 140 (2020).

56. W. Wei, P. Tang, Z. Xie, Y. Li, and R. Wang, “Dynamic imaging and quantification of subcellular motion with eigen-decomposition optical coherence tomography-based variance analysis,” J. Biophotonics 12(10), 1 (2019).